Porous Cooling and Thermoelectric Generation in Concentrated Photovoltaic Thermal Systems

Abhishek Gupta[a], Sandesh S. Chougule[b], Sandip K. Saha[a,†]

[a]Department of Mechanical Engineering, Indian Institute of Technology Bombay, Mumbai - 400076, India.

[b]Clean Energy Processes (CEP) Laboratory, Department of Chemical Engineering, Imperial College London, London- SW72AZ, United Kingdom.

N.B.: This is the ACCEPTED MANUSCRIPT version of this article. The final published version of the article can be found at: https://doi.org/10.1016/j.applthermaleng.2025.128451

Abstract

Photovoltaic-thermal systems under high concentrated solar radiation suffer severe thermal management challenges, as elevated cell temperatures degrade electrical output and material reliability. This study evaluates the thermoelectric and photovoltaic performance of a high concentrated photovoltaic-thermal system integrated with a spectral splitter and hybrid cooling configuration, comprising a porous heat sink and a thermoelectric generator module. A coupled electro-thermal-fluid model is developed to assess the various performance parameters of the hybrid system. The effect of critical design parameters, including porosity, pore size, and inlet velocity, is investigated. The cell maximum temperature surpasses the critical threshold of 110 °C for the porosities above 0.8. A reduction in porosity enhances the temperature uniformity across the photovoltaic cell surface. Conversely, increasing the porosity of the heat sink leads to an improvement in the overall exergy performance of the system. Variations in pore size insignificantly affect the electrical output of the photovoltaic cell. However, increased pressure drop at low pore sizes results in a sharp reduction in the overall exergy. The overall exergy reduces from 49.29% at a pore size of 3.5 mm to 42.59% at a pore size of 1.5 mm for a porosity of 0.66. The increased coolant inlet velocity reduces the overall exergy despite aiding in temperature control, suggesting that operation at lower inlet velocities is optimal. The overall exergy increases to 52.76% at 0.4 m/s from 49.29% at 0.8 m/s inlet velocity. The thermoelectric generator modules help improve the overall exergy by converting excess waste heat into useful electrical energy output.

Keywords: Porous medium; Thermoelectric generator; Efficiency; Exergy; Stress; High concentrated photovoltaic cell; Hybrid cooling

Corresponding author: †sandip.saha@iitb.ac.in

Nomenclature

A	Solar cell area (m^2)
C_f	Inertial constant
c_p	Specific heat (J/kg·K)
CR	Concentration ratio
d_p	Pore size
EX	Exergy (W)
E	Young's modulus of the bulk solid (Pa)
$\tilde{E}$	Young's modulus of the porous structure (Pa)
FI	Failure Index
G	Net concentrated solar irradiation (W/m^2)
h	Convective heat transfer coefficient ($W/m^2 \cdot K$)
I	Filtered solar irradiation (W/m^2)
I_g	Electric current in thermoelectric generator (A)
k	Thermal conductivity (W/m·K)
K	Permeability
P	Power (W)
q	Heat generation (W/m^3)
Q	Energy (W)
T	Temperature (°C)
ΔT	Temperature difference (°C)
U	Superficial velocity
u	Pore velocity
V	Solar cell volume (m^3)
$\vec{V}$	Velocity vector (m/s)

Greek symbols

α	Absorptivity
σ	Stefan-Boltzmann constant ($W/m^2 \cdot K^4$)
ρ	Water density (kg/m^3)
μ	Viscosity of water (Pa·s)
v	Poisson ratio
β_T	Cell temperature coefficient
η	Efficiency (%)
ζ	Exergy Efficiency (%)
α_T	Thermal expansion coefficient (K^{-1})
σ_T	Thermal stress (Pa)
ϕ	Porosity
λ	Wavelength (nm)
τ	Maximum crushing stress of the bulk solid (Pa)
$\tilde{\tau}$	Maximum crushing stress of the porous structure (Pa)

Subscript

cell	PV cell
Ge	Germanium
a	ambient
el	electrical
Cu	Copper
f	fluid
fric	frictional
max	maximum
ref	reference

eff	effective
conv	convection
out	outlet
in	inlet
rad	radiation
opt	optical
th	thermal
m	mean
Ce	Ceramic
al	aluminium
o	overall

Abbreviations

CTE	Coefficient of thermal expansion
TEG	Thermoelectric generator
CPV	Concentrated photovoltaic
JI	Jet impingement
HTC	Heat transfer coefficient
CJI	Confined jet impingement
HCPV	Highly concentrated photovoltaic
PV	Photovoltaic
HCPV-T	Highly concentrated photovoltaic thermal

1. Introduction

Photovoltaic (PV) cells harness the photovoltaic effect to transform sunlight into electricity. Recognized as a sustainable and eco-friendly energy solution, PV technology is instrumental in meeting the world's growing energy needs while helping to lower greenhouse gas emissions. However, conventional PV systems are limited by relatively low energy conversion efficiencies. A significant portion of incident solar energy remains unused in the form of heat, and elevated operating temperatures further reduce electrical output. To improve the overall energy efficiency of solar systems, photovoltaic-thermal (PV-T) technology has been developed. Hybrid systems combine PV panels with thermal collectors to produce both electrical power and thermal energy concurrently. By removing excess heat from the PV cells, PV-T systems improve overall energy conversion while simultaneously reducing cell temperatures, enhancing electrical performance and extending component lifespan.

Concentrated photovoltaic-thermal (CPV-T) systems further advance this concept by incorporating optical concentrators such as Fresnel lenses, parabolic troughs, or compound parabolic concentrators to focus sunlight onto a smaller PV area. This concentration increases the irradiance on the PV surface, thereby enhancing electrical and thermal output. CPV-T systems can deliver higher energy densities, making them suitable for high-performance solar applications. However, the use of concentrated solar flux leads to significantly elevated temperatures at the PV surface. Gupta et al.[1] reported that the T_{cell} can increase above 600 °C above a CR of 500. Elevated temperatures negatively impact PV cell performance by lowering the open-circuit voltage and diminishing total power generation. Under a concentration ratio (CR) of 200, the PV module's conversion efficiency drops by about 0.098% for each 1 °C increase in cell temperature [2]. Moreover, sustained thermal stress can cause material fatigue, delamination, and accelerated ageing of encapsulants and adhesives within the module. Therefore, thermal management becomes a crucial aspect of CPV-T system design. Efficient

cooling strategies are essential not only to preserve electrical efficiency but also to ensure the long-term durability and reliability of the system.

Various cooling methods, such as thermoelectric cooling (TEC) [3][4], heat pipe cooling [5], liquid immersion method, phase change material (PCM) cooling, nanomaterials [6][7], micro-channel cooling [8][9], jet impingement [10], and porous materials [11], have been used by several researchers. Passive cooling methods refer to thermal management strategies that operate without external power input or active mechanical systems. In PV cell cooling applications, such methods include radiative heat dissipation, natural convection, PCM cooling, heat pipe, spectral splitting, and thermoelectric cooling. The TEGs are useful in the conversion of waste heat into electrical power. Chen et al. [12] reported a detailed numerical study on thermal-concentrated solar TEGs, highlighting how geometric optimization and thermal concentration ratios influence system efficiency. Sabry et al.[13] investigated a hybrid system combining CPV cells with TEGs to cool the PV cell and recover waste heat simultaneously. Their study used both simulations and experiments to evaluate various TEG configurations and demonstrated a net power gain of up to 7.4% over standalone CPV systems. The results underscore the viability of passive cooling through TEG integration without compromising overall energy output. Kohan et al. [3] presented a 3-D numerical model to simulate the behaviour of a PV-TEG hybrid system. They found that although the hybrid system can outperform a standalone PV under certain conditions, the performance gain is marginal due to limited temperature differentials across the TEG. The study also highlighted how cooling efficiency and TEG configuration significantly influence the overall system output, especially under concentrated solar input. Various researchers have investigated the spectral splitting techniques to maintain the PV cell temperature within acceptable limits. Spectral splitters divide sunlight into distinct wavelength ranges, directing only the portions that effectively

generate electron-hole pairs toward the photovoltaic cell [14][15]. This selective transmission enhances conversion efficiency by reducing thermal losses.

Literature shows that the passive cooling techniques alone are insufficient to maintain optimal temperatures in CPV-T systems due to high heat fluxes generated under concentrated sunlight [16]. Effective thermal management typically requires active or hybrid cooling strategies to ensure efficient performance and prevent overheating. Many researchers have investigated that jet impingement (JI) cooling improves heat dissipation in CPV-T systems by using high-speed fluid jets, thereby increasing the convective HTC[17]. Royne et al. [18] proposed a JI-based cooling system to manage the thermal load of closely spaced PV cells operating under high solar concentration, demonstrating its effectiveness in maintaining high heat transfer rates while minimizing pumping power. Gupta et al.[1] investigated various channel designs and found that the mini-channel configuration achieved the best performance, lowering the cell temperature to 54 °C while maintaining a pressure drop of 163 Pa under *CR* 1000. Various researchers have evaluated the effect of flow in a porous medium on the PV-T system performance. Kiwan et al. [11] investigated employing porous materials to improve the thermal management of PV panels, demonstrating that porous fins and layers significantly enhance PV efficiency by improving heat dissipation under mixed convection conditions. Their study highlighted the effectiveness of porous media in reducing operating temperatures, with efficiency improvements of up to 9.19% compared to non-porous configurations. Masalha et al. [19] investigated enhancing PV panel performance using porous media-integrated cooling channels. The study reported a reduction in surface temperature of up to 35.7% and an improvement in power output by 9.4%, showcasing the effectiveness of optimized porous structures in thermal regulation. Salman et al. [20] studied using porous media flow at the rear side of photovoltaic cells to improve thermal management. Their findings showed that integrating porous structures led to a T_{cell} reduction of approximately 9–14 °C, thereby

enhancing the overall performance of the PV system. Poudel et al. [21] explored the thermal regulation of PV panels using a porous nanochannel device integrated into the rear surface. The system achieved an average T_{cell} reduction of 31.5 °C and enhanced electrical power output by approximately 33%.

It can be concluded from the literature that passive cooling techniques often fall short under high thermal loads, especially in HCPV-T configurations, where elevated temperatures severely degrade efficiency. Therefore, active cooling becomes essential for effective thermal management in HCPV-T systems. Incorporating a porous heat sink offers a promising solution to maintain PV cell temperatures within safe limits and enhance overall system efficiency. The literature shows that the HCPV-T system waste heat can be harnessed and converted into supplementary electrical energy through the use of a TEG module. This enhances the overall energy output without requiring extra solar input. Furthermore, the literature indicates that spectral splitters can selectively transmit the portion of solar radiation that is effective for power generation. Photons within the 300–1100 nm range are primarily responsible for generating electron-hole pairs in PV cells, while the remaining spectrum contributes mainly to heating. [22].

Despite the numerous strategies for regulating the thermal conditions of CPV-T systems, several research gaps persist. The current literature largely focuses on either standalone or dual-component cooling systems limited to TEG+PCM cooling [23], heat pipe and PCM cooling [24], CJI and TEG cooling[25], microchannels and JI cooling [26], PCM and JI cooling [27], and heat pipe and JI cooling [28]. Most dual-component cooling strategies have been applied to non-concentrated or low-concentrated PV systems. Hence, their applicability under high concentration remains underexplored. The mechanical implications of thermal stress distribution and failure mechanism are studied only briefly. There is a lack of comprehensive parametric investigations reported in the literature to examine the impact of

pore size, porosity, and inlet velocity on the hybrid HCPV-T+TEG system performance. In contrast, the present study introduces a triple-hybrid configuration—combining a porous heat sink, a spectral splitter, and TEG modules for HCPV–T systems, which has not been evaluated previously in the literature. The application of the hybrid cooling strategies in the context of high solar concentration is reported. Thus, overcoming the current limitation where most such methods are used only in low-concentration or non-concentrated PV-T systems. Unlike prior studies, a comprehensive parametric optimization of the porous media (pore size, porosity, inlet velocity) tailored to the high flux regime is performed, while simultaneously evaluating coupled PV, TEG, and coolant performance. Furthermore, this work extends beyond existing approaches by integrating a coupled exergy analysis and thermal stress reliability assessment, enabling energetic performance prediction and insights into mechanical durability under extreme conditions. Thus, the novelty of this study lies in proposing the triple-hybrid HCPV–T configuration (porous heat sink + spectral splitter + TEG modules) at high concentration ratios. Porous media cooling, when optimized, is demonstrated to maintain PV temperatures below a critical threshold even at 1000 suns. Moreover, a system-level exergy–mechanical analysis is provided**,** which has been largely absent in prior CPV–TEG works. This work quantitatively links the porous heat sink design parameters with system exergy, thereby providing practical design guidelines for reliable and efficient photovoltaic-thermal operation under high concentration.

2. System Details

The present study investigates the performance of a hybrid HCPV-T + TEG system integrated with an aluminium-based porous heat sink for enhanced thermal management. The configuration comprises a PV cell, a Direct Bonded Copper (DBC) assembly, a spectral splitter, thermoelectric generator (TEG) modules, and a forced convection cooling mechanism utilizing a porous medium. The photovoltaic (PV) cell has dimensions of 70 × 70 mm with 90% optical

efficiency and is exposed to concentrated solar irradiance corresponding to a *CR* of 1000. A 150 × 150 mm copper-ceramic-copper assembly is placed beneath the solar cell to support the structure. A porous heat sink with an area of 150 × 150 mm, fabricated from aluminium due to its structural integrity and high thermal conductivity, is placed directly beneath the DBC assembly. The porous aluminium structure improves heat dissipation by expanding the effective surface area for convective HT and disrupting thermal boundary layers. A coolant is actively circulated through this porous domain to maintain the operating temperatures of the PV module within acceptable limits. To utilize a portion of the waste heat generated, four TEG modules, each measuring 20 × 20 mm, are embedded within the porous aluminium heat sink. This is achieved by providing dedicated slots in the porous structure to accommodate the TEGs. The top surface of each TEG is placed in direct thermal contact with the rear side of the DBC assembly. The lateral and bottom surfaces of the TEG modules are in direct contact with the surrounding porous medium, enabling effective heat extraction from the cold side via the circulating coolant. This configuration ensures optimal thermal coupling between the PV, TEG, and cooling subsystems while maintaining structural integration within the porous domain. A glycol-ZnO nanofluid-based spectral splitter is placed above the PV cell, allowing only a fraction of concentrated solar irradiation in the 300-1100 nm wavelength range to be transmitted [22][29]. A gap is maintained between the spectral splitter and the PV cell [29]. Hence, the effects of the temperature of the spectral splitter on the system performance are not considered in this study. The validity of this assumption is analysed in Appendix A. It is found that a slight increase in the maximum cell surface temperature of 0.2 °C is obtained if the spectral splitter is attached to the PV cell.

A fraction of the transmitted solar irradiation is converted into electrical energy by the PV cell, depending on the cell electrical efficiency. The unused portion is converted into heat and transferred through conduction to the DBC assembly. The top surfaces of the TEGs are in

direct thermal contact with the DBC layer. These TEGs utilize the conducted heat to generate electricity by exploiting the Seebeck effect. The residual heat, remaining after the TEGs and DBC assembly, is further transferred to a porous aluminium heat sink. Finally, the heat is dissipated through convective heat transfer using a coolant fluid circulating through the porous structure. Tables 1 and 2 present the dimensions and thermophysical characteristics of the solar cell and its associated layers, respectively.

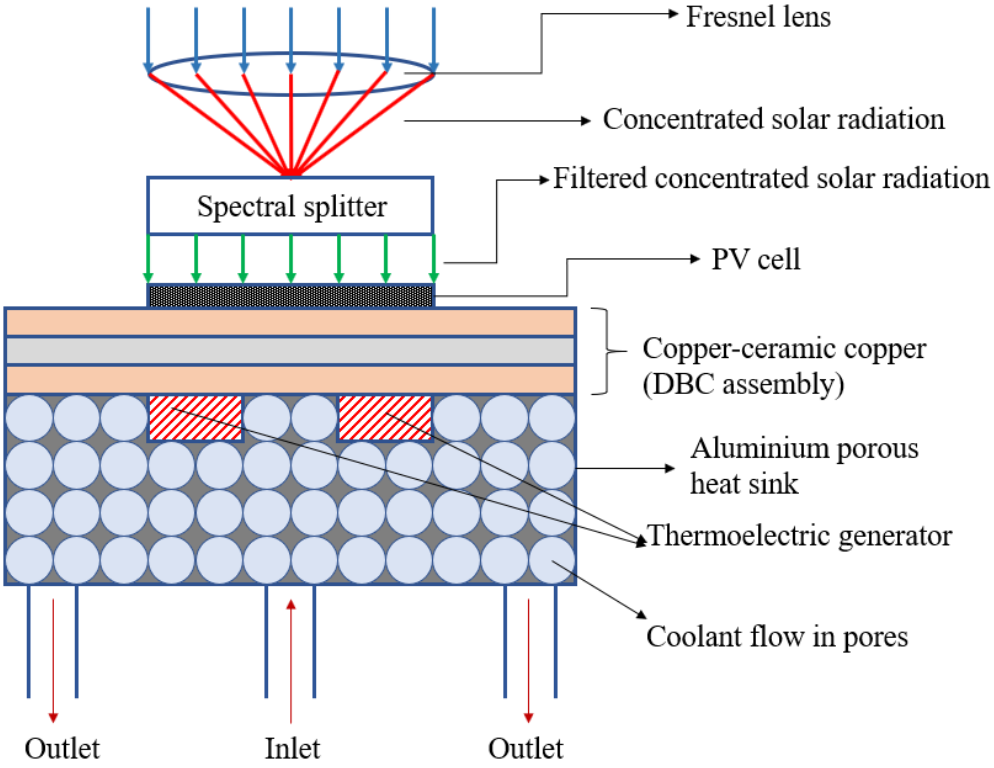


Figure 1: HCPV-T system equipped with spectral splitter, TEG modules, and porous heat sink

Table 1: Dimensions of the heat sink, DBC assembly, and solar cell

Layer	**Width (mm)**	**Thickness (mm)**	**Length (mm)**
Porous heat sink	150	12	150
TEG modules	20	3	20

Copper-1 and 2	150	0.25	150
Ceramic	150	0.32	150
Germanium	70	0.19	70

Table 2: Thermophysical properties of the system [30][31]

Layer	**Emissivity (ε)**	**Specific heat (c_p) (J/kg·K)**	**Density (ρ) (kg/m^3)**	**Thermal conductivity (k) (W/m·K)**
Germanium	0.9	320	5323	60
TEG module (Bismuth-Telluride)	0.66	550	4100	1.45
Ceramic	0.75	900	3900	30
Copper	0.05	385	8700	400
Aluminium	0.9	871	2719	202.6
Coolant fluid (water)	-	4182	998	0.6

3. Governing equations

A steady-state 3-D numerical model is developed to analyze the conjugate heat transfer and fluid flow within the system comprising a PV cell, DBC assembly, TEG modules and aluminium porous heat sink to evaluate key performance indicators such as cell temperature, power output from PV and TEGs, pressure drop, and exergy efficiency over a range of coolant velocities and porous medium configurations. The model captures the absorption of solar radiation by the PV layer, conductive heat transfer through the solid regions, convective cooling in the porous aluminium heat sink, and thermoelectric conversion in the TEG modules. The distribution of filtered concentrated solar irradiation is assumed to be uniform on the PV cell

surface. This assumption is widely adopted in both numerical and experimental studies by employing solar simulators or metal halide lamps to maintain uniform irradiation [32][33]. In outdoor experiments, the solar irradiance varies with time and weather, which may lower the electrical output compared to the present predictions. However, the relative performance trends with respect to input parameters will remain valid in all conditions. A porous heat sink is attached beneath the DBC assembly. The coolant flow within the porous structure is considered incompressible, steady, and Newtonian fluid. The TEG modules are attached between the porous heat sink and the DBC assembly. The constant thermophysical properties of all layers are assumed in the current study. This assumption has also been used in previous studies of CPV and CPV-TEG systems [3]. The validity of this assumption can be observed in the model validation section.

3.1 Heat conduction in the PV cell and DBC assembly

The heat conduction through each layer is governed as [34],

$$k_i \nabla^2 T_i + q_i = 0 \tag{1}$$

where, k_i denotes the thermal conductivity of the i^{th} layer. q_i denotes the heat generation in the layers. q_i is taken as zero in the DBC assembly layers. The q_{Ge} is dependent on η_{cell} and is given as [34],

$$q_{Ge} = \frac{(1 - \eta_{cell}) \cdot G \cdot \alpha_{Ge} \cdot A}{V} \tag{2}$$

The total concentrated solar irradiance transmitted through the spectral splitter is represented by G. A denotes the cell surface area, and V denotes the PV cell volume. α_{Ge} is the PV cell absorptivity. η_{cell} denotes the PV cell electrical efficiency. The fraction (1- η_{cell}) is transformed into heat and is responsible for internal heat generation.

The total concentrated solar radiation is given as,

$$G = I \cdot CR \cdot \eta_{opt} \tag{3}$$

where, I denotes the filtered solar radiation after the spectral splitter, which is considered to be uniformly distributed over the PV cell. The value of I is obtained by integrating the standard AM1.5G solar spectrum (ASTM G173-03, 2012) over the specified wavelength range. CR is taken as 1000, and η_{opt} is taken as 0.9 in the current study.

$$I = \int_{\lambda_{min}}^{\lambda_{max}} E_{sun}(\lambda) \cdot \tau_{ss}(\lambda) d\lambda \tag{4}$$

where, $E_{sun}(\lambda)$ is the spectral irradiance, and $\tau_{ss}(\lambda)$ is the spectral transmissivity of the splitter [29].

The cell electrical efficiency (η_{cell}) is expressed as,

$$\eta_{cell} = \eta_{ref} - \beta_T (T_{cell} - T_{ref}) \tag{5}$$

where, η_{ref} is taken as 40.3% at CR = 1000, and T_f= 298 K. β_T is the thermal coefficient and is considered to be 0.047% [36].

3.2 Flow model and heat transfer model in porous heat sink

The flow in the porous structure is assumed to be an incompressible, steady and Newtonian fluid. The thermophysical properties of the coolant are considered to be isotropic.

Continuity equation:

$$\rho_f \nabla \cdot (U) = 0 \tag{6}$$

Momentum equation:

$$\frac{1}{\phi}\rho_f((U.\nabla)U) = -\nabla P + \nabla.\left[\frac{\mu}{\phi}(\nabla U + (\nabla U)')\right] - \left(\frac{\mu}{K}U + \frac{C_f}{\sqrt{K}}\rho_f U^2\right) \tag{7}$$

The Darcy-Forchheimer-Brinkman equation is used to account for the effects of porous media on fluid flow. The Darcy term $\left(\frac{\mu}{K}U\right)$ adds a linear resistance to the flow, the Forchheimer term $\left(\frac{C_f}{\sqrt{K}}\rho_f U^2\right)$ adds inertial resistance to the flow, and the Brinkman term $\left[\frac{\mu}{\phi}(\nabla U + (\nabla U)')\right]$ accounts for the viscous shear stress. The porosity of the heat sink is denoted by ϕ. Porosity is defined as the void fraction of the porous heat sink medium through which the coolant flows. U is the superficial velocity and is calculated as $U = \phi \cdot u$, where the pore velocity is denoted

by u. ρ_f and μ refer to the density and viscosity of the coolant. The permeability is denoted by K, and C_f is the inertial constant [37].

$$K = \frac{{d_p}^2}{1039 - 1002\phi} \tag{8}$$

$$C_f = \frac{0.5138\ \Phi^{-5.739}}{d_p}\sqrt{K} \tag{9}$$

The pore size is denoted by d_p.

Energy equation:

Solid phase $$\nabla \cdot (k_{es}\nabla T_s) + h_v\left(T_f - T_s\right) + S_{rad} = 0 \tag{10}$$

Liquid phase $$\rho c_{pf} U \cdot \nabla T_f = \nabla \cdot \left(k_{ef}\nabla T_f\right) + h_v(T_s - T_f) \tag{11}$$

where, S_{rad} denotes the radiation heat transfer inside the porous structure. The temperature of the porous structure is below 100 °C. Hence, the S_{rad} is neglected in the current study [38]. The k_{ef}, and k_{es} are given as:

$$k_{ef} = \phi k_f \tag{12}$$

$$k_{es} = (1 - \phi)k_s \tag{13}$$

The energy equation is coupled via a convective HTC term, h_v [39].

For $0.66 < Re < 0.93$ $$Nu_{s,f} = \frac{h_v d_p}{k_f} = 0.52\ Re^{0.5} Pr^{0.37} \tag{14}$$

$$\text{Reynolds number, } Re = \frac{\rho U d_p}{\mu} \tag{15}$$

3.3 Thermal and electrical power

The electrical power generated by the PV cell is obtained as [40],

$$P_{el} = \eta_{cell} \cdot G \cdot \alpha_{Ge} \cdot A \tag{16}$$

The pumping power losses can be obtained as,

$$P_{fric} = \frac{\dot{m}}{\rho_f}\Delta P \tag{17}$$

where, the pressure drop in the porous structure is denoted as ΔP.

The thermal power (Q_{th}) output and thermal efficiency (η_{th}) are expressed as [41],

$$Q_{th} = \dot{m} C_{p,f} (T_{f,out} - T_{f,in}) \tag{18}$$

$$\eta_{th} = \frac{Q_{th}}{I \cdot CR \cdot \eta_{opt} \cdot A} \tag{19}$$

where, at the outlet and inlet, the coolant temperature is denoted by $T_{f,out}$ and $T_{f,in}$, respectively.

3.4 Thermal stress in the PV cell

The thermal stress in the PV cell layer is estimated as [42],

$$\sigma_T = E_{Ge} \cdot \Delta\alpha_T \cdot \frac{(T_R - T)}{(1 - \nu_{Ge})} \tag{20}$$

$$\Delta\alpha_T = \alpha_{T,Ge} - \alpha_{T,Cu} \tag{21}$$

where, $\alpha_{T,i}$ denotes the CTE of i^{th} layer. E_{Ge} is the cell Young's modulus. The reference temperature, T_R is taken as 25 °C. ν_{Ge} is the Ge layer Poisson ratio.

Table 4. Properties of Ge and Cu layers[43]

$\alpha_{T,Ge}$ (K^{-1})	$\alpha_{T,Cu}$ (K^{-1})	E_{Ge} (GPa)	E_{Cu} (GPa)	ν_{Ge}	ν_{Cu}
6.1×10^{-6}	17×10^{-6}	102.7	110	0.28	0.34

3.5 Failure index (*FI*) of porous structure

Temperature gradients within the solid portion of the porous material can induce thermal stresses, which, if sufficiently high, may cause structural failure of the porous medium. The *FI* is estimated as the ratio of the maximum stress experienced by the porous structure and the maximum allowable stress. The structure mechanically fails when $FI \geq 1$.

$$FI = \max\left(\frac{\tau_i}{\tau_s}\right) \tag{22}$$

The maximum crushing stress of the porous structure is estimated as [44],

$$\frac{\tilde{\tau}}{\tau} = 0.2\,(1 - \phi)^{\frac{3}{2}} \tag{23}$$

where, $\tilde{\tau}$ is the maximum crushing stress of the porous structure, and τ is the maximum crushing stress of the bulk solid. The Young's modulus of the porous structure is given as,

$$\frac{\tilde{E}}{E} = (1-\phi)^2 \tag{24}$$

3.6 TEG model

The heat conduction in the TEG is expressed as:

$$k\nabla^2 T - P_{gen} = 0 \tag{25}$$

where, P_{gen} represents the specific power generated by the TEG module. The P_{gen} can be estimated using the following relation:

$$P_{TEG} = Q_h - Q_c \tag{26}$$

$$P_{TEG} = P_{gen} \cdot V_{TEG} \tag{27}$$

where, the heat supplied to and extracted from the TEG module are represented by Q_h and Q_c, respectively, while V_{TEG} denotes the volume of the TEG module.

The heat supplied and extracted at TEG junctions is estimated as [45][46],

$$Q_h = n \cdot \epsilon_t \cdot I_g \cdot T_h + K \cdot \Delta T - \frac{1}{2} {I_g}^2 R \tag{28}$$

$$Q_c = n \cdot \epsilon_t \cdot I_g \cdot T_c + K \cdot \Delta T + \frac{1}{2} {I_g}^2 R \tag{29}$$

where, n denotes the p-n junction pairs in the TEG module, and is considered as 128. The average Seebeck coefficient, ε_t, is taken as 282 μV/K. T_c corresponds to the temperatures at the cold and hot sides of the TEG, respectively. I_g represents the electric current flowing through the TEG, and R is its electrical resistance. The temperature difference across the TEG module is indicated by ΔT.

The I_g, and R of the TEG module are given as [47]:

$$I_g = \frac{n \cdot \varepsilon_t \cdot (T_h - T_c)}{R(1+\mu)} \tag{30}$$

$$R = 10^{-5} \times (-3)(T_m - 273)^2 - 0.0133(T_m - 273) + 1.542 \tag{31}$$

where, μ represents the ratio between the external load resistance and the internal resistance of the TEG module, while T_m denotes the average temperature between the hot and cold junctions. The electrical efficiency of the TEG can be calculated using the following expression. [46]:

$$\eta_{TEG} = \frac{{I_g}^2 \cdot R_L}{Q_h} \tag{32}$$

where, R_L denotes the load resistance.

3.7 Thermal and electrical exergies

Thermal exergy represents the portion of thermal energy (heat) that can be converted into useful work under ideal conditions, relative to a reference environment. Thermal exergy of the hybrid HCPV-T+TEG system is written as [48],

$$EX_{th} = \dot{m}_f c_f (T_{f,out} - T_{f,in}) \left(1 - \frac{T_o}{T_m}\right) \tag{33}$$

$$T_m = \frac{(T_{f,out} - T_{f,in})}{\ln\left(\frac{T_{f,out}}{T_{f,in}}\right)} \tag{34}$$

where, the reference temperature, T_o is 298 K. The electrical energy is a high-grade energy. It can be fully utilized and is considered pure exergy. Hence, the net electrical power output from the hybrid HCPV-T+TEG system is considered electrical exergy.

3.8 Boundary conditions

The top surfaces of the PV cell and DBC assembly are exposed to the ambient. Hence, the boundary conditions at the exposed surfaces are given as.

$$-k_i \frac{\partial T_i}{\partial z} = q_{rad,i\to S} + q_{conv,i\to a} \tag{35}$$

where, $q_{rad,i\to S}$ denoted the radiative losses from i^{th} layer and $q_{conv,i\to a}$ denotes convective heat losses from i^{th} layer to the ambient. The losses are calculated as [30],

$$q_{conv,i\to a} = h_{conv,wind}(T_i - T_a) \tag{36}$$

$$h_{conv,wind} = 5.82 + 4.07 V_{wind} \tag{37}$$

$$q_{rad,i\to S} = \sigma\epsilon_i(T_i^4 - T_s^4) \quad (38)$$

$$T_s = 0.0522T_a^{1.5} \quad (39)$$

where, T_i represents the temperature of the top surface of the i^{th} layer. V_{wind} is the wind velocity and is taken as 1m/s. ε_i is the emissivity of the i^{th} layer. T_s is the sky temperature.

The sides of all the layers are given convective boundary conditions. The interfaces between all the layers are assigned thermally coupled interface conditions.

$$-k_m\nabla T_m = -k_n\nabla T_n \text{ and } T_m = T_n \quad (40)$$

At inlet: T_{in} = 298 K, and $V_f = V_{in}$.

At outlet: Gauge pressure = 0

The numerical simulations are performed using ANSYS Fluent 2021 R2. The governing equations for energy, momentum, and continuity are discretized using a second-order upwind scheme, and the solution is advanced using the coupled algorithm to ensure stability and accuracy. Convergence criteria are set to 10^{-8} for the energy equation, 10^{-6} for momentum, and 10^{-3} for the continuity equations. To account for the temperature-dependent heat generation within the PV cell, a user-defined function (UDF) is implemented. This UDF introduces a volumetric source term in the energy equation based on the functional relationships defined in Equations (2) and (4). Additionally, the thermal–electrical behaviour of the TEG module is captured through a separate UDF. This function computes the source term using Equations (26), (28), and (29), based on the ΔT_{TEG}. During each iteration, the UDF retrieves the face temperature of the TEG module and updates the corresponding energy source term, enabling a dynamic, temperature-coupled solution. A flow chart of the numerical simulation procedure and UDF compilation is illustrated in Figure 2.

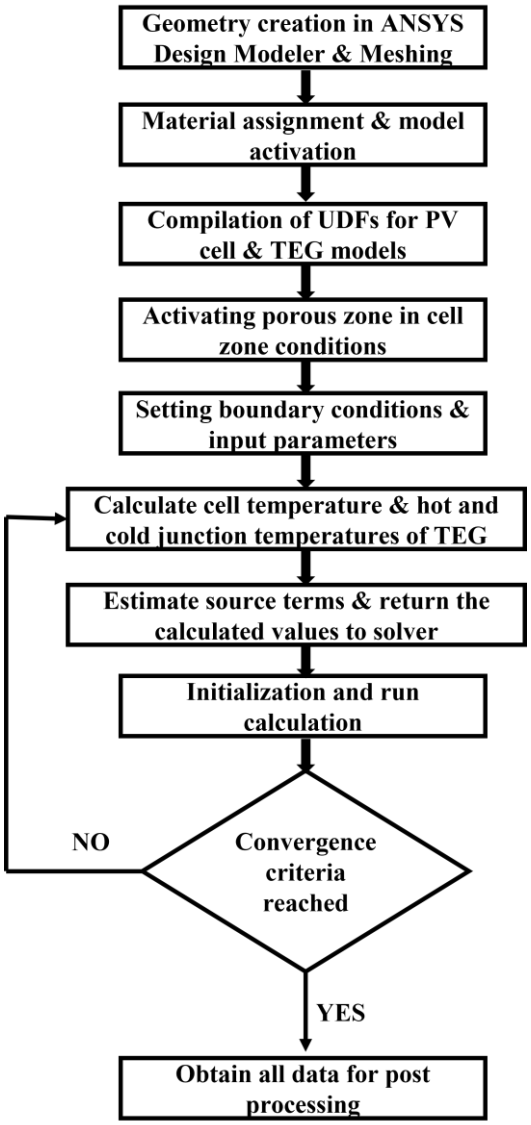
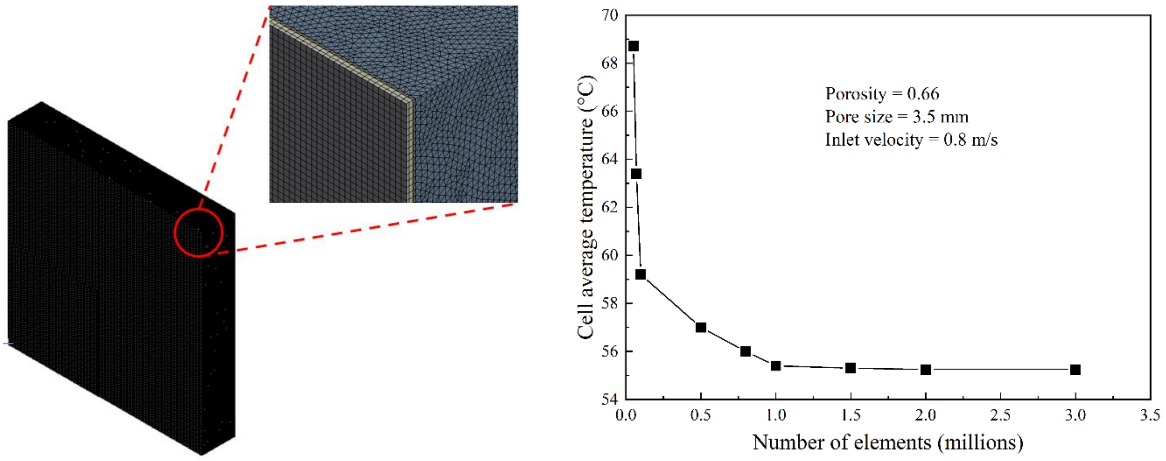


Figure 2: Flow chart of the simulation procedure

3.9 Mesh sensitivity analysis

To verify the accuracy and stability of the numerical results, a mesh sensitivity analysis is performed for a representative case with porosity = 0.66, pore size = 3.5 mm, and inlet velocity = 0.8 m/s. Figure 3(a) shows the meshed geometry. The study involves systematically refining the mesh and evaluating its effect on the predicted T_{cell}. The results demonstrate a consistent convergence trend, with the variation in T_{cell} diminishing progressively as the mesh is refined. Beyond 1.5 million elements, the relative change in the T_{cell} drops below 0.09%, indicating that further refinement has a negligible impact on the solution. This confirms that a mesh size

corresponding to approximately 1.5 million elements is sufficient to achieve mesh-independent results for the chosen configuration. The mesh independence is also supported by Figure 3(b), which clearly exhibits asymptotic behaviour at higher mesh densities.



(a) (b)

Figure 3: (a) Meshed geometry, (b) mesh sensitivity test for porosity = 0.66, pore size = 3.5 mm and inlet velocity = 0.8 m/s

3.10 Validation of TEG model, cell model, and porous heat sink model

The numerical models for the TEG module, PV cell, and fluid flow and heat transfer in porous structures are validated against the established literature and manufacturer datasheets to ensure model accuracy. Figure 4(a) shows the validation of the TEG model with the module datasheet provided by CUSTOM THERMOELECTRIC, LLC [31]. The model demonstrates a good agreement with the module datasheet in the range of 30 °C to 80 °C with a maximum error of less than 6%. The error increases at higher temperature differences due to the assumption of constant thermophysical properties. In particular, the Seebeck coefficient and thermoelectric material vary with temperature, which has a minor influence at lower ΔT_{TEG}, but becomes more significant at higher ΔT_{TEG}. However, in the present study, the maximum ΔT_{TEG} remains below 65 °C. Therefore, the model is sufficiently accurate for analyzing the thermal management and power generation in the CPV-TEG system. Figure 4(b) illustrates the cell model validation with the results reported by Theristis et al. [16]. The author analyzed the temperature of a multi-

junction solar cell under varying convective HTC on the rear side of the DBC substrate, simulating different ambient conditions. The present model successfully replicates the temperature trends, maintaining a maximum error of 3.9%. Figures 4(c) and 4(d) depict the validation of the flow and heat transfer model inside a porous medium subjected to uniform heat flux, with the results obtained by Lu et al. [39]. The comparison reveals a good agreement, with the model predicting pressure drop and radial temperature distribution with maximum errors of 2.7% and 5%, respectively.

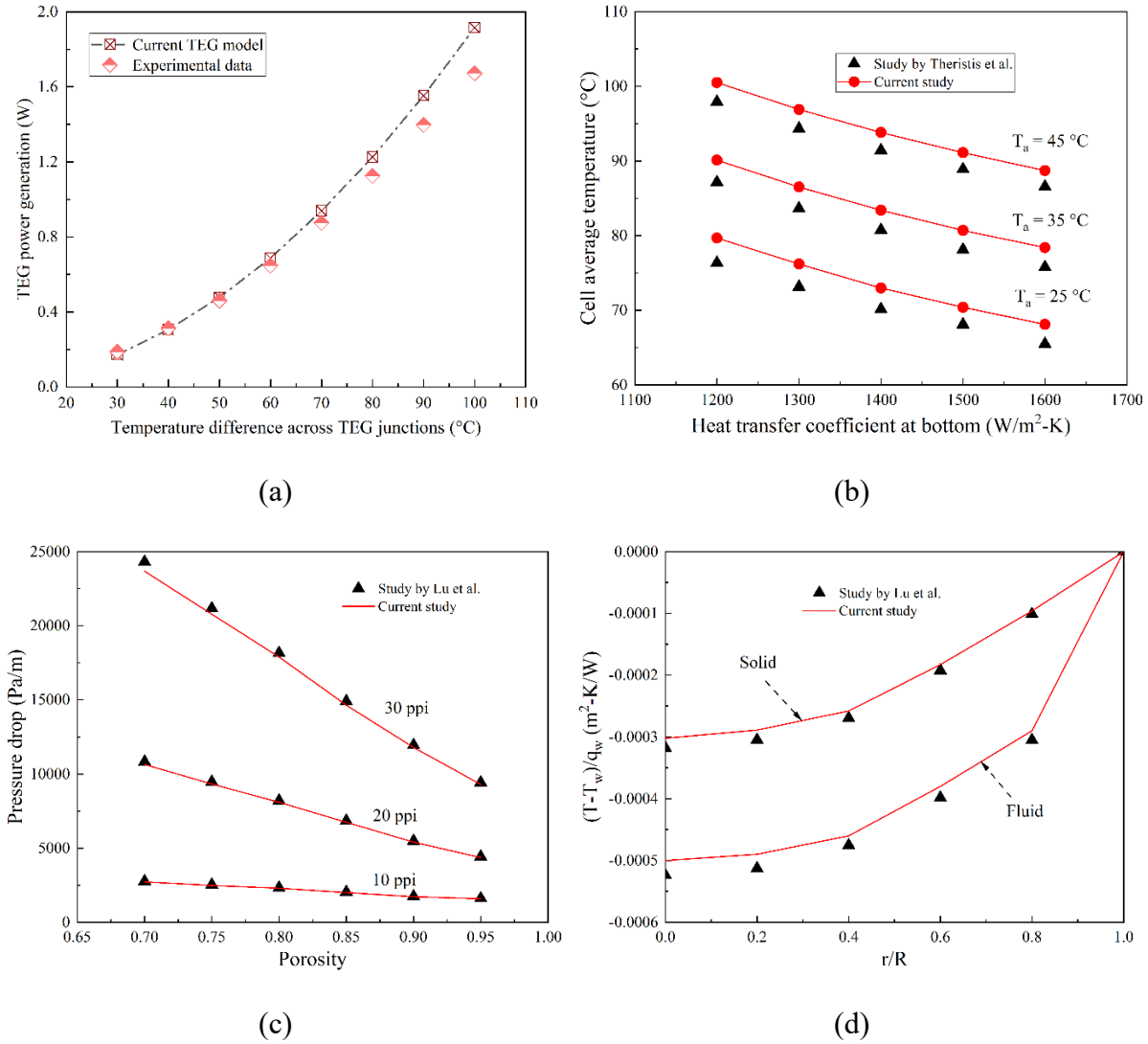


Figure 4: Validation of (a) TEG model, (b) PV cell model, (c) flow model, (d) heat transfer model

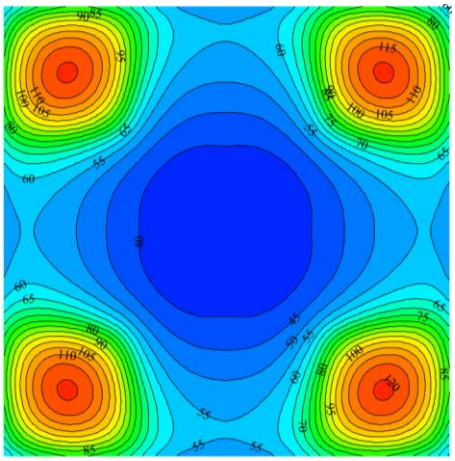
4. Results and Discussion

The thermal and electrical performance of a hybrid HCPV-T+TEG system cooled by a porous heat sink is comprehensively analyzed in this study using a square aluminium porous heat sink directly beneath the PV cell and DBC substrate assembly. The cooling fluid is introduced centrally into the heat sink and exits symmetrically through four outlets located at the corners. Four TEG modules are strategically embedded between the DBC layer and the heat sink. These modules are arranged so that their hot sides maintain direct thermal contact with the DBC layer, while both the lateral surfaces and cold sides interface with the porous heat sink to facilitate efficient heat extraction. The influence of key design parameters such as the porosity of the heat sink, pore size, and inlet coolant velocity is systematically evaluated to determine their impact on the overall energy and exergy efficiency and thermal regulation of the hybrid system.

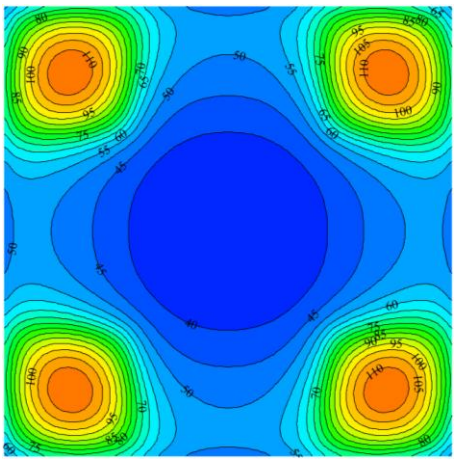
4.1. Effect of Porosity

Figure 5 displays the temperature distribution over the PV cell top surface for the porosities of 0.9, 0.85, 0.8, 0.75, 0.7, and 0.66, respectively. It is found that the T_{max} appears at the corners of the PV cell, where the TEG modules are installed. As the TEG modules have low thermal conductivity, the heat transfer from the bottom copper layer to the aluminium heat sink is limited in these regions. This leads to a localized rise in temperature at the TEG positions. The low thermal conductivity of the TEGs also contributes to a progressive increase in thermal resistance from the centre of the cell toward its corners. The inlet is placed at the centre of the heat sink. The kinetic energy of the coolant is converted into pressure energy at the centre, resulting in a high HTC at the centre. Hence, the cell temperature is minimal at the centre. Also, higher temperature gradients across the PV cell surface are observed at higher porosities of the heat sink. It is attributed to the reduced effective thermal conductivity and diminished heat-spreading capability of the porous medium at high porosity. As porosity increases, the proportion of solid material within the structure decreases, leading to a lower effective thermal

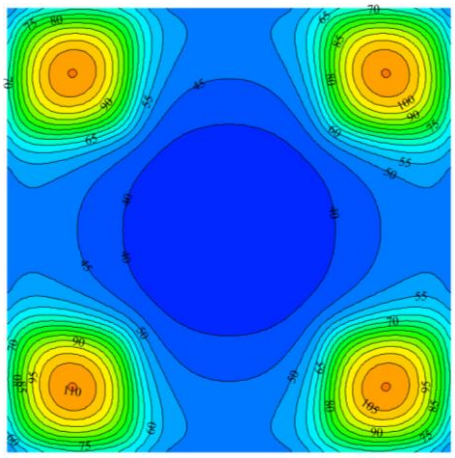
conductivity. This limits the ability of the medium to conduct heat uniformly across the contact surface with the PV cell. It results in less uniform cooling due to uneven fluid distribution within the porous domain. These effects combine to produce localized regions of varying temperature, thereby increasing the thermal gradient across the cell surface.



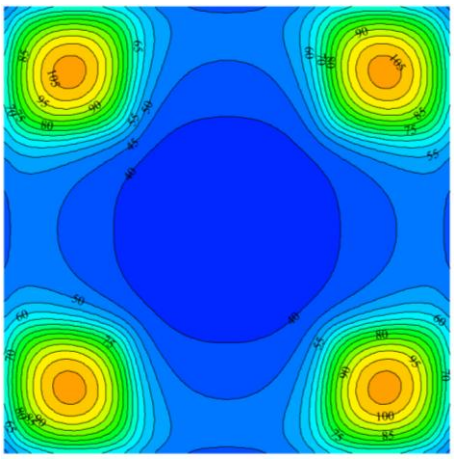
(a)



(b)



(c)



(d)

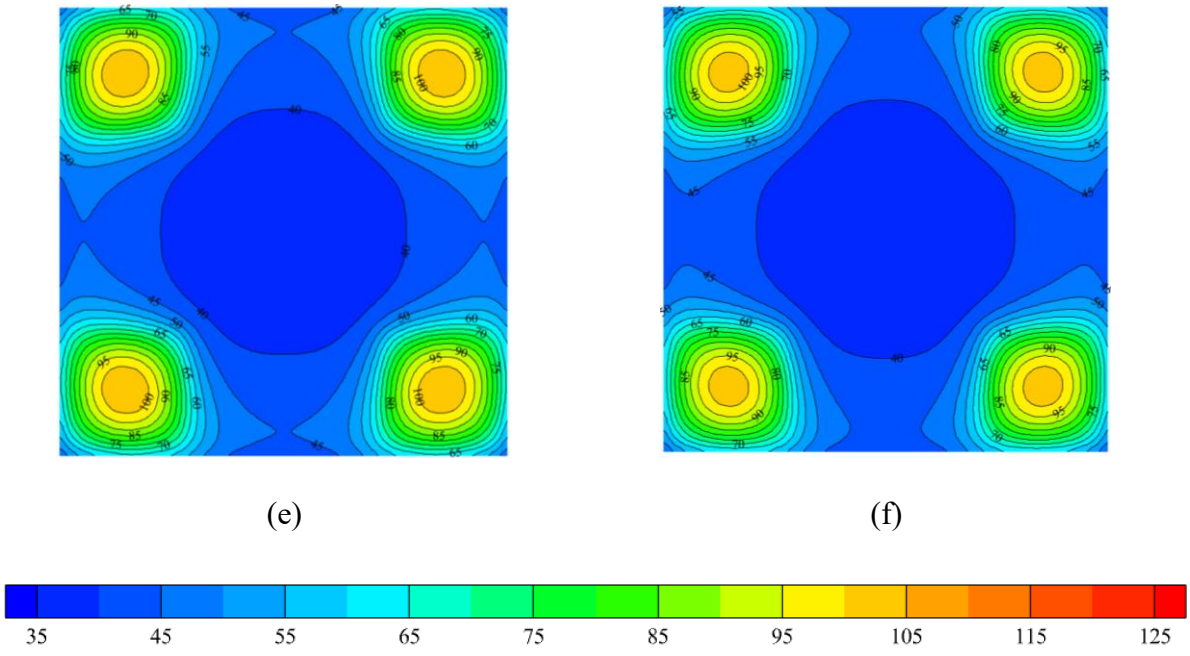


Figure 5: Effect of porosity on temperature distribution over the PV cell top surface for ϕ = (a) 0.9, (b) 0.85, (c) 0.8, (d) 0.75, (e) 0.7, (f) 0.66

Figure 6 shows the variation in T_{max}, ΔP, and FI with the porosity of the medium at inlet velocity = 0.8 m/s, and d_p = 3.5 mm. The T_{max} over the cell surface is 103.5 °C, 104.8 °C, 107.3 °C, 110 °C, 114.4 °C, and 120.8 °C for the porosity of 0.66, 0.7, 0.75, 0.8, 0.85, and 0.9, respectively. It can be observed that T_{max} increases with an increase in the porosity of the heat sink. The low porosity of the medium denotes the presence of more solid material in the medium. This results in a better thermal pathway for the heat conduction from the DBC assembly to the porous heat sink. Hence, the thermal resistance decreases with low porosities of the heat sink. The effective thermal conductivity of the medium increases with decreasing porosity, resulting in better heat transfer and a reduced cell maximum temperature. It can be observed that the T_{max} increases beyond the temperature constraint of 110 °C for the porosities of 0.9 and 0.85. The ΔP is 6406 Pa, 4703 Pa, 3425 Pa, 2562 Pa, 2016 Pa, and 1630 Pa for the porosities of 0.66, 0.7, 0.75, 0.8, 0.85, and 0.9, respectively. It has been found that the pressure drop (ΔP) reduces as the ϕ increases. The volume of the flow path available for fluid flow reduces with decreased porosity. It results in a higher flow resistance for the cooling fluid in

the flow path. The decreased porosity of the medium also results in a low permeability, resulting in an increased ΔP. The failure index (FI) of the porous structure is 0.211, 0.207, 0.204, 0.197, 0.190, and 0.178 for the porosities of 0.66, 0.7, 0.75, 0.8, 0.85, and 0.9, respectively. The failure index of the porous structure decreases as the porosity of the medium increases. The effective Young's modulus of the porous structure increases with a decrease in ϕ as the material becomes denser and more structurally continuous with a decrease in porosity, leading to an increase in σ_t generation in the structure. The yield stress limit of the structure also increases with a reduction in porosity. However, the ratio of generated thermal stress to yield limit, i.e., FI increases with the low porosity of the medium.

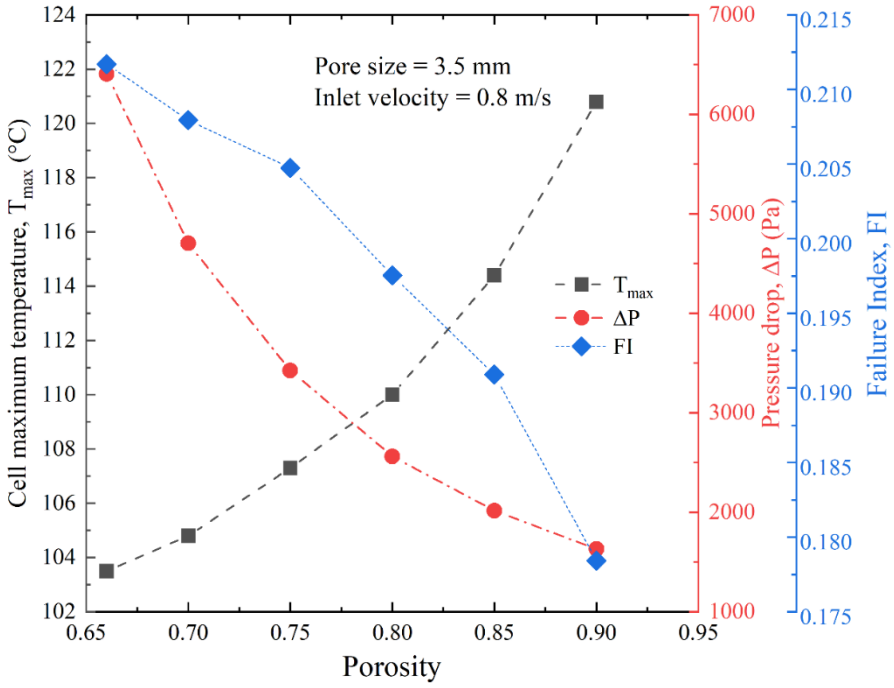


Figure 6: Variation in T_{max}, ΔP and FI with heat sink porosity

Figure 7 shows the variation in T_{cell}, η_{cell}, and η_{th} with the porosity of the medium at inlet velocity = 0.8 m/s, and d_p = 3.5 mm. The T_{cell} over the cell surface is 55.25 °C, 56.18 °C, 57.8 °C, 59.66 °C, 62.53 °C, and 67 °C for the porosities of 0.66, 0.7, 0.75, 0.8, 0.85, and 0.9, respectively. The T_{cell} increases as the porosity of the heat sink increases. The high porosity results in lower heat conduction from the bottom copper layer to the heat sink, resulting in an increase in T_{cell}. The η_{cell} is 38.87%, 38.83%, 38.75%, 38.67%, 38.53%, and 38.32% for the

porosity of 0.66, 0.7, 0.75, 0.8, 0.85, and 0.9, respectively. The η_{cell} depends on the cell operating temperature. The open-circuit voltage of the PV cell decreases with rising temperature, resulting from the increase in intrinsic carrier concentration. The short-circuit current increases slightly with temperature due to the lower bandgap. However, the gain in short-circuit current is marginal compared to the loss in open-circuit voltage. Hence, the η_{cell} decreases with an increase in T_{cell}. The η_{th} is 54.54%, 54.58%, 54.66%, 54.74%, 54.88%, and 55.1% for the porosity of 0.66, 0.7, 0.75, 0.8, 0.85, and 0.9, respectively. The η_{th} increases with an increase in the porosity of the heat sink. The η_{cell} reduces with increased porosity, indicating that a larger portion of the incident energy is transformed into heat rather than electrical power. This results in improved thermal efficiency of the HCPV-T system at higher porosities.

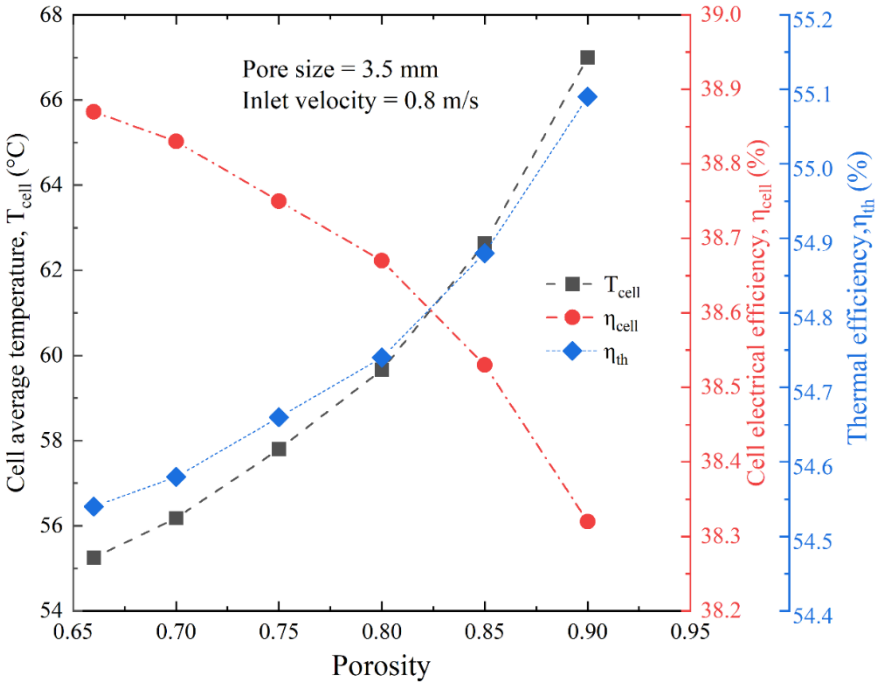


Figure 7: Variation in T_{cell}, η_{cell}, and η_{th} with heat sink porosity

Figure 8 shows the variation in the ΔT_{TEG}, P_{TEG}, and η_{TEG} with the porosity of the medium at inlet velocity = 0.8 m/s, and d_p = 3.5 mm. The ΔT_{TEG} is 48 °C, 49.3 °C, 51.5 °C, 54 °C, 57.9 °C, and 63.4 °C for the porosity of 0.66, 0.7, 0.75, 0.8, 0.85, and 0.9, respectively. It is observed that the ΔT_{TEG} increases with the porosity of the heat sink. The thermal resistance between the bottom copper layer and the heat sink is highest at the TEG locations, resulting in

minimal heat conduction at those locations. This leads to a high temperature at the TEG hot junction. In contrast, the TEG module's cold junction is attached to the heat sink, leading to a high ΔT_{TEG}. As the porosity increases, the cell temperature at the TEG location also increases, resulting in a higher T_h. In contrast, the temperature of the TEG cold junction also increases with increased porosity. However, the increase in T_c of the TEG module is marginal as compared to the increase in T_h. Hence, the temperature difference across TEG junctions increases with increased porosity. The P_{TEG} is 4.03 W, 4.31 W, 4.87 W, 5.53 W, 6.76 W, and 8.97 W for the porosity of 0.66, 0.7, 0.75, 0.8, 0.85, and 0.9, respectively. The P_{TEG} increases with increasing porosity of the heat sink. The P_{TEG} is a function of the current flowing in the TEG module. The current flowing through the module also rises with an increased ΔT_{TEG}, thereby enhancing the electrical power generated. The η_{TEG} increases from 1.21% to 1.93 % for an increase in porosity from 0.66 to 0.9. The η_{TEG} is the ratio of P_{TEG} and the heat input at the hot junction of the TEG module. Both the power generation and the heat absorbed at the hot junction increase with increasing porosity. However, the relative increase in P_{TEG} is more significant at higher ΔT_{TEG}, leading to a net increase in thermoelectric efficiency.

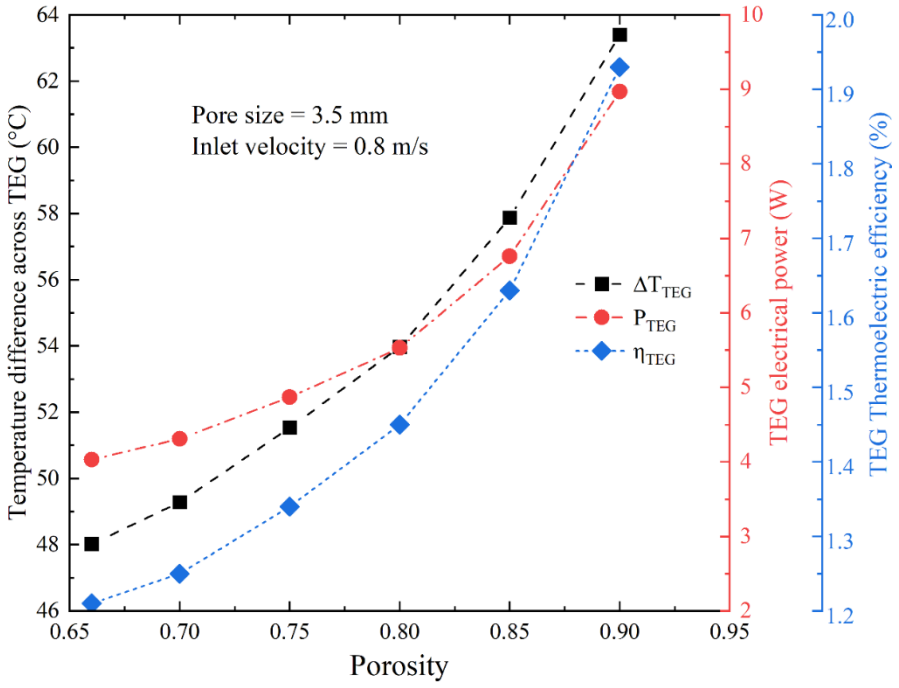


Figure 8: Variation in ΔT_{TEG}, P_{TEG}, and η_{TEG} with heat sink porosity

Figure 9 shows the variation in the ζ_{el}, ζ_{th}, and ζ_o with the porosity of the medium at inlet velocity = 0.8 m/s, and d_p = 3.5 mm. The ζ_{el} of the system is 34.31%, 35.53%, 36.41%, 36.98%, 37.3%, and 37.45% for the porosity of 0.66, 0.7, 0.75, 0.8, 0.85, and 0.9, respectively. The ζ_{el} increases as ϕ increases. Electrical energy can be considered a high-grade energy and pure exergy. The ζ_{el} accounts for the net electrical power generated from the HCPV-T+TEG hybrid system and the electrical power loss due to the pumping of coolant fluid. Figure 7 shows that the η_{cell} decreases with increased porosity of the medium. Hence, the HCPV-T system's electrical power output also decreases with increasing porosity of the heat sink. Additionally, Figure 6 shows that the ΔP decreases with the porosity of the heat sink. Hence, the pumping power losses due to frictional pressure drop also decrease with increased porosity. In contrast, the P_{TEG} increases with an increase in the porosity of the heat sink. Hence, the ζ_{el} shows the overall trade-off between η_{cell}, ΔP, and P_{TEG}. The ζ_{th} is 14.98%, 15%, 15.04%, 15.09%, 15.17%, and 15.28% for the porosities of 0.66, 0.7, 0.75, 0.8, 0.85, and 0.9, respectively, which depicts that the ζ_{th} increases with the porosity of the heat sink. The ζ_{th} accounts for the maximum useful work that can be extracted from the η_{th} of the HCPV-T system. The maximum amount of useful work is constrained by the available temperature of thermal energy. A comparison between Figure 7 and Figure 9 indicates that for the porosity of 0.9, only 15.28% of the total 55.1% thermal output is effectively utilized for useful work. The ζ_o is 49.29%, 50.53%, 51.46%, 52.08%, 52.47%, and 52.74% for the porosity of 0.66, 0.7, 0.75, 0.8, 0.85, and 0.9, respectively. This indicates that the ζ_o increases with the porosity of the heat sink. The ζ_o denotes the total useful work obtained from the HCPV-T system, combining the ζ_{el} and ζ_{th}.

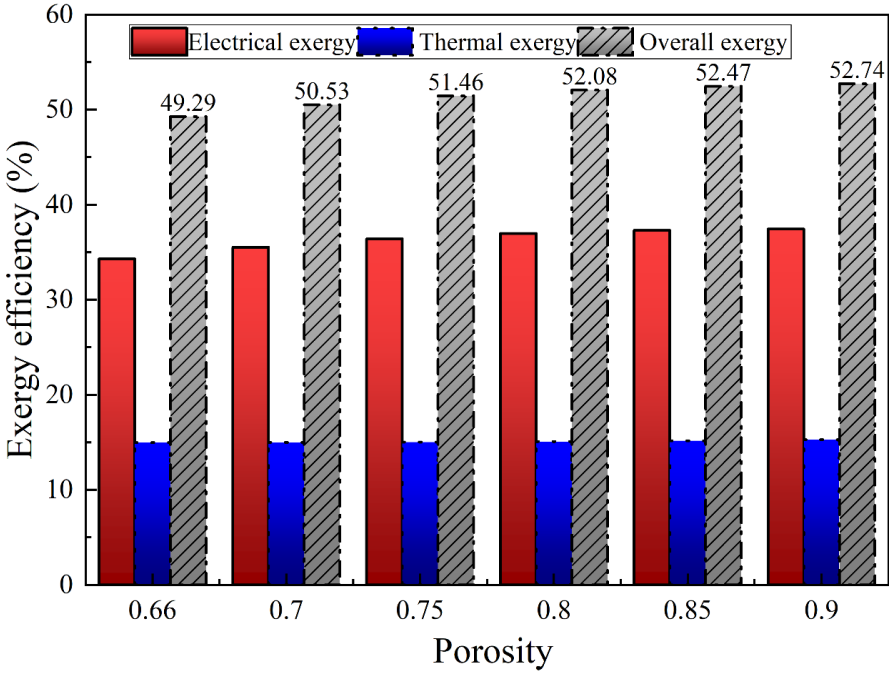


Figure 9: Variation in ζ_{el}, ζ_{th}, and ζ_o with heat sink porosity

Figure 10(a) shows the σ_t distribution across the cell diagonal for ϕ = 0.66. The σ_t is 15.42 MPa at the cell centre and increases to 121.42 MPa at 25 mm, and 90.59 MPa at 30 mm along the cell diagonal line. The PV cell layer is directly attached to the DBC assembly. The high-temperature gradients on the PV cell exist due to the presence of the TEG module and uniform heat generation inside the solar cell, leading to the σ_t generation across the cell surface. The σ_t is minimal in the vicinity of the cell centre and corners. The cell temperature is lowest at the centre due to the coolant inlet at the centre, leading to minimal thermal stress. However, the σ_t increases along the diagonal line due to increased temperature gradients away from the centre. The σ_t increases rapidly after 15 mm and is highest at 25 mm along the diagonal line. The local cell temperature is significantly higher at those locations due to the lower thermal conductivity of the TEG module.

Figure 10(b) depicts the σ_{max} variation with the porosity of the medium at inlet velocity = 0.8 m/s, and d_p = 3.5 mm. The σ_{max} is 122 MPa, 124 MPa, 127.9 MPa, 132.1 MPa, 139 MPa, and 148.9 MPa for the porosity of 0.66, 0.7, 0.75, 0.8, 0.85, and 0.9, respectively. The σ_{max} increases as ϕ increases. The local cell temperature at TEG locations increases with the porosity

of the heat sink, leading to an increase in σ_{max}. The yielding stress of the Ge cell is 135 MPa. The σ_{max} is beyond the yielding limit of the PV cell for the porosities of 0.85 and 0.9. Hence, the heat sink with porosities of 0.85 and 0.9 cannot be used to cool the current HCPV-T system used in this study.

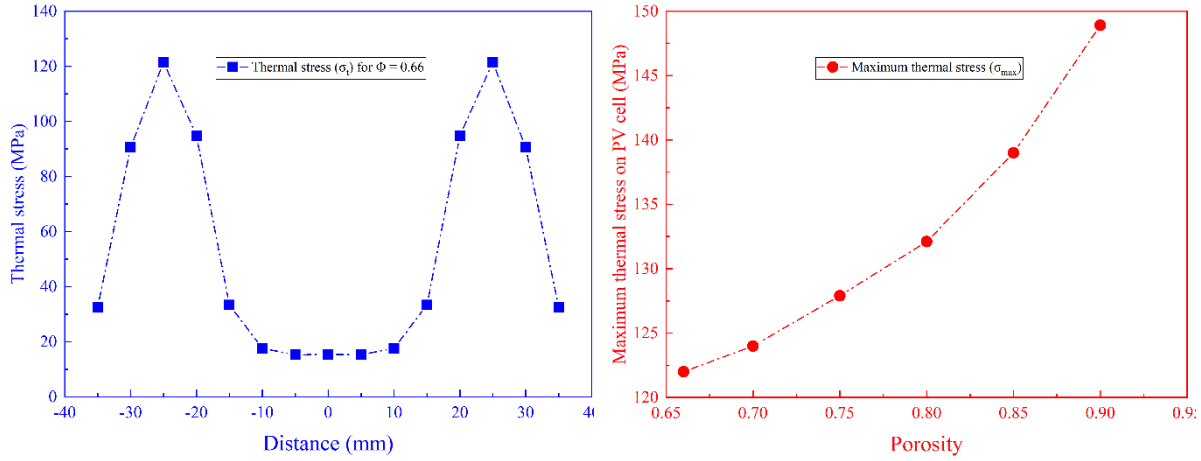


Figure 10: Variation in (a) σ_t across the cell diagonal for $\phi = 0.66$ and (b) maximum thermal stress on the PV cell with porosity of the heat sink

4.2. Effect of pore size

Figure 11 depicts the variation in the T_{max}, ΔP, and FI with the pore size at inlet velocity = 0.8 m/s, and $\phi = 0.66$. The T_{max} increases from 102.2 °C to 103.5 °C for the increase in d_p from 1.5 to 3.5 mm, respectively. A smaller pore size provides a higher surface area per unit volume for the heat exchange. It also allows better heat conduction through the solid matrix, leading to a higher thermal dispersion. The convective HTC between the solid matrix and coolant fluid also increases with a reduced pore size, leading to an enhanced heat exchange. Hence, T_{max} reduces with a decrease in the pore size of the heat sink. A comparison of T_{max} from Figures 6 and 11 shows that porosity has a greater influence on the T_{max} than pore size. The porosity governs the solid-fluid conduction balance and changes the amount of fluid that can take away the heat from the PV cell. A decrease in porosity increases the solid fraction, thereby improving the conduction pathways. It also reduces the coolant flow volume, thereby affecting the convective heat transfer. This dual impact of porosity on both conduction and convection makes it a more

dominant factor in governing T_{max}, whereas the pore size primarily modifies the convective surface area without substantially altering the conduction-convection balance. The ΔP decreases from 15517 Pa to 6406 Pa for the increase in d_p from 1.5 to 3.5 mm, respectively. The ΔP increases sharply with a decrease in pore size. Since the permeability $\propto$ (pore size)^2, it leads to a sharp decline with a reduction in pore size, resulting in a higher viscous flow resistance. The inertial resistance of the flow also increases as the flow becomes more constricted with a reduced pore size, leading to a sharp increase in ΔP. A comparison of ΔP from Figure 6 and Figure 11 shows that the pressure drop is affected more by pore size than porosity. The change in pore size produces a quadratic effect on the permeability of the medium, while the influence of porosity on permeability is nonlinear but comparatively less steep. It leads to a lesser effect of porosity on flow resistance. The failure index (FI) of the porous structure increases from 0.202 to 0.211 for the increase in d_p from 1.5 to 3.5 mm, respectively. The thermal gradients in the porous structure increase as d_p increases, leading to increased thermal stress generation inside the porous structure. It results in an increase in FI for larger pore sizes.

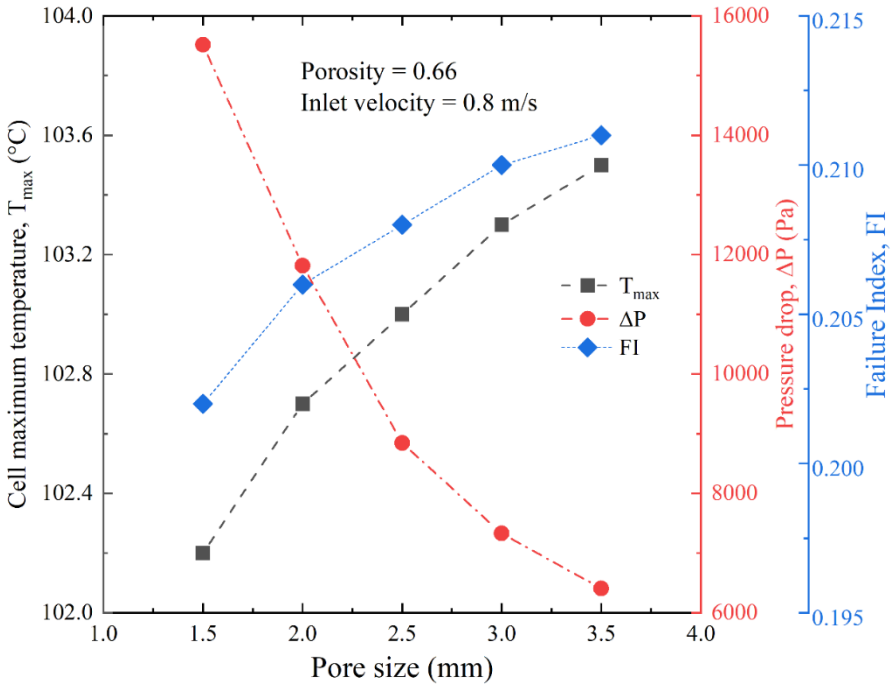


Figure 11: Variation in T_{max}, ΔP, and FI with pore size

Figure 12 displays the variation in the T_{cell}, η_{cell}, and η_{th} with the pore size at inlet velocity = 0.8 m/s, and ϕ = 0.66. The T_{cell} increases from 54.4 °C to 55.25 °C for the increase in d_p from 1.5 to 3.5 mm, respectively. The smaller pore sizes allow the disruption of the thermal boundary layer more frequently, enhancing heat transfer. It leads to better temperature uniformity and reduced T_{cell}. The η_{cell} decreases from 38.91% to 38.87% for the increase in d_p from 1.5 to 3.5 mm, respectively. The reduction in η_{cell} is very marginal. The η_{th} increases from 54.50% to 54.54% for the increase in d_p from 1.5 to 3.5 mm, respectively. The η_{th} increases marginally with an increase in pore size. It is evident from Figure 12 that pore size has a very marginal effect on η_{cell} and η_{th}.

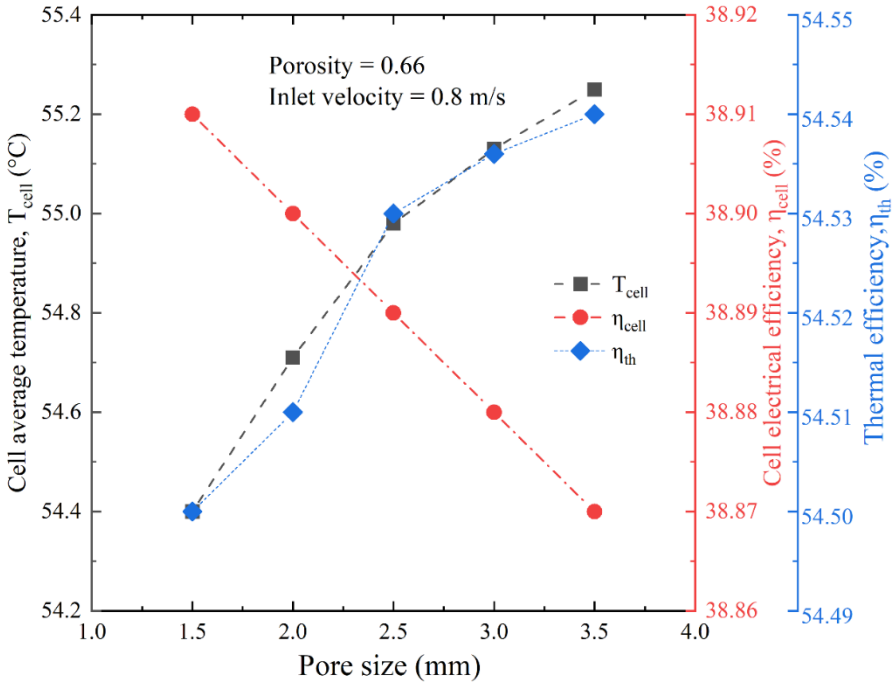


Figure 12: Variation in T_{cell}, η_{cell} and η_{th} with pore size

Figure 13 shows the variation in the ΔT_{TEG} and P_{TEG} with the pore size at inlet velocity = 0.8 m/s, and ϕ = 0.66. The ΔT_{TEG} increases from 46.96 °C to 48 °C for the increase in d_p from 1.5 to 3.5 mm, respectively. The T_h and T_c of the TEG module increase with an increase in pore size due to decreased heat transfer at larger pore sizes. However, the TEG module's hot junction is attached to the DBC assembly, leading to a higher rise in T_h. The P_{TEG} increases from 3.79

W to 4.03 W for the increase in d_p from 1.5 to 3.5 mm, respectively. The TEG module generates more power when the electrical load resistance matches the internal resistance. Also, the electrical current in the TEG module increases with an increase in ΔT_{TEG}, leading to more power generation at larger pore sizes. The η_{TEG} increases from 1.16% to 1.21% for the increase in d_p from 1.5 to 3.5 mm, respectively. The increase in ΔT_{TEG} results in an increased P_{TEG}, thereby increasing thermoelectric efficiency at larger pore sizes.

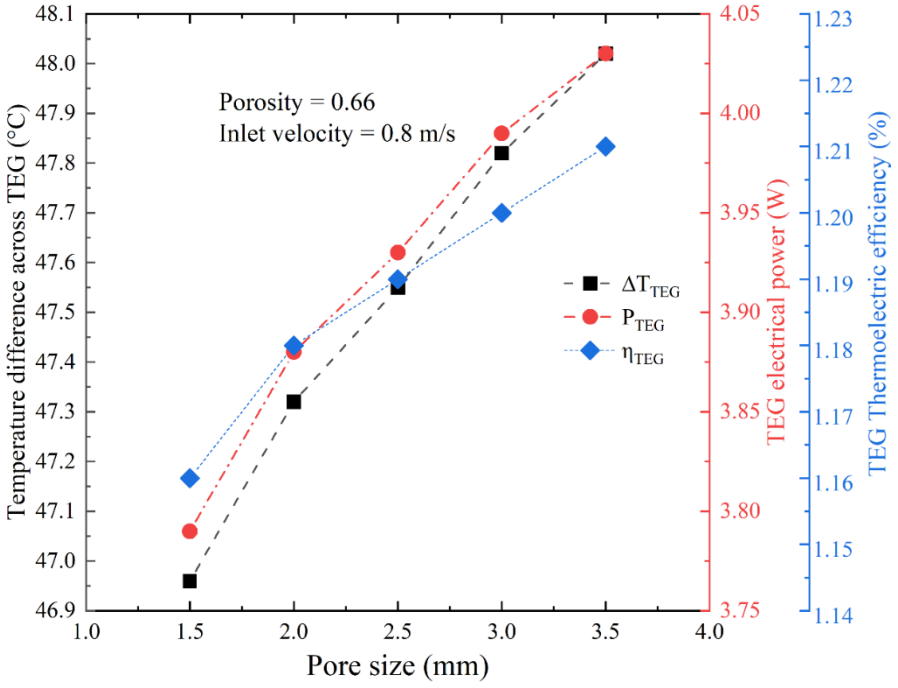


Figure 13: Variation in ΔT_{TEG}, P_{TEG}, and η_{TEG} with pore size

Figure 14 shows the variation in the ζ_{el}, ζ_{th}, and ζ_o with the pore size at inlet velocity = 0.8 m/s, and $\phi = 0.66$. The ζ_{el} increases from 27.63% to 34.31% for the increase in d_p from 1.5 to 3.5 mm, respectively. The ζ_{el} increases with an increase in the pore size of the medium. The ζ_{el} serves as an indicator of the balance between η_{cell}, ΔP, and P_{TEG}. The η_{cell} and P_{TEG} are marginally affected by the pore size, as illustrated in Figures 12 and 9, respectively. However, the ΔP is highly sensitive to pore size, primarily due to the sharp decline in permeability of the medium at smaller pore sizes, as shown in Figure 11. The overall trade-off results in a sharp decrease in ζ_{el} at smaller pore sizes. A comparison of Figure 9 and Figure 14 illustrates that the ζ_{el} is more affected by the pore size than by the porosity of the heat sink. The ζ_{th} increases from

14.96% to 14.98% for the increase in d_p from 1.5 to 3.5 mm, respectively. The ζ_{th} is marginally affected by the change in pore sizes. The ζ_o increases from 42.59% to 49.29% for the increase in d_p from 1.5 to 3.5 mm, respectively. The ζ_o increases as the pore size increases. The ζ_o accounts for the combined trade-off between cell electrical power, pumping power losses, TEG electrical power, and thermal power output. A higher overall exergy efficiency implies higher productivity and more usable energy. Hence, larger pore sizes are recommended for the thermal management of the hybrid HCPV-T+TEG system employed in the current study.

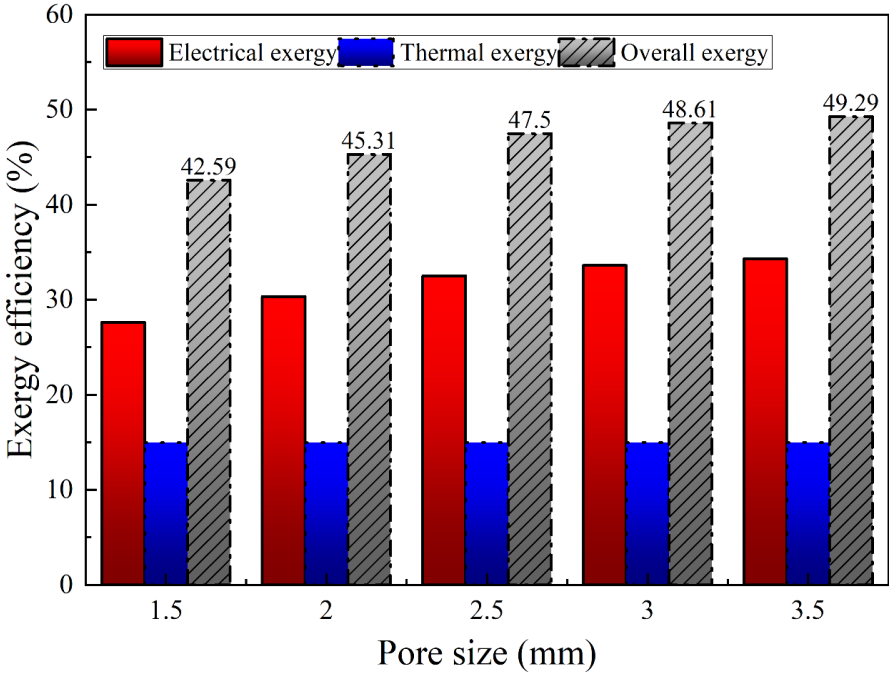


Figure 14: Variation in ζ_{el}, ζ_{th}, and ζ_o with pore size

4.3. Effect of inlet velocity

Figure 15 shows the variation in the T_{max}, ΔP, and FI with the inlet velocity at $\phi = 0.66$, and $d_p = 3.5$ mm. The T_{max} is 110.9 °C, 108.4 °C, 106.5 °C, 105 °C, and 103.5 °C for the inlet velocities of 0.4, 0.5, 0.6, 0.7, and 0.8, respectively, which indicates that the T_{max} decreases with an increase in inlet velocity of the coolant fluid. This can be primarily attributed to the intensified convective heat transfer within the porous structure. As the velocity rises, the convective HTC increases, thereby improving the system's ability to dissipate heat from the solar cell through the underlying layers, including the TEG and porous heat sink. Additionally, the increased flow

rate lowers the overall thermal resistance of the cooling path, facilitating more effective heat removal. Hence, the temperature gradient between the solar cell and the cooling medium becomes steeper, promoting more efficient thermal management. It is also observed that the T_{max} reaches beyond the temperature constraint of 110 °C at an inlet velocity = 0.4 m/s. Hence, the flow velocity below 0.4 m/s cannot be used for the thermal management of the HCPV-T system shown in the current study.

The ΔP is 1568 Pa, 2381 Pa, 3364 Pa, 4515 Pa, and 6406 Pa for the inlet velocities of 0.4, 0.5, 0.6, 0.7, and 0.8, respectively. The ΔP increases with an increase in coolant inlet velocity. This rise in ΔP is attributed to the nonlinear relationship between flow resistance and velocity. As the fluid velocity increases, both viscous and inertial effects become more pronounced, particularly in porous structures where flow paths are highly tortuous. According to the Forchheimer equation, which extends Darcy's law to account for inertial effects, the ΔP is a function of the linear (viscous) and quadratic (inertial) terms of velocity. Consequently, the inertial losses dominate at higher inlet velocities, leading to a disproportionately higher pressure drop across the medium. The *FI* of the porous structure is 0.261, 0.245, 0.232, 0.222, and 0.211 for the inlet velocities of 0.4, 0.5, 0.6, 0.7, and 0.8, respectively. The *FI* decreases as the coolant inlet velocity increases. The thermal gradients across the porous structure reduce with increased coolant velocity due to enhanced convective HTC. As a result, the thermal stresses across the porous structure also reduce, reducing *FI*.

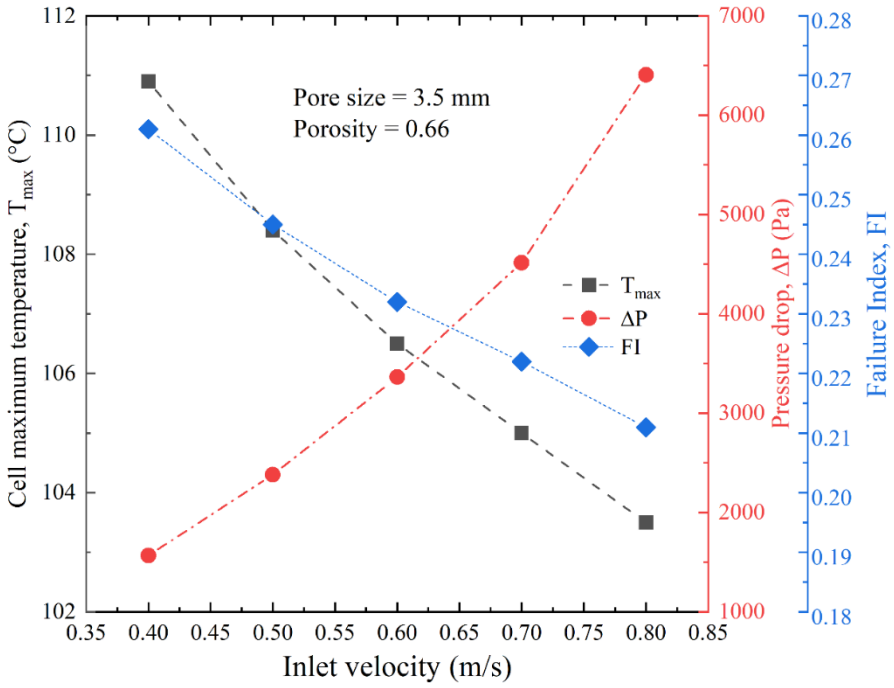


Figure 15: Variation in T_{max}, ΔP, and FI with inlet velocity

Figure 16 illustrates the variation in T_{cell}, η_{cell}, and η_{th} with the inlet velocity at $\phi = 0.66$, and d_p = 3.5 mm. The T_{cell} is 61.6 °C, 59.9 °C, 57.8 °C, 56.5 °C, and 55.25 °C for the inlet velocities of 0.4, 0.5, 0.6, 0.7, and 0.8, respectively. The T_{cell} reduces with an increase in V_{in}. As the fluid velocity increases, the convective HTC rises due to improved momentum exchange near the boundary layer, which becomes thinner and improves heat extraction. The η_{cell} is 38.58%, 38.66%, 38.75%, 38.82%, and 38.87% for the inlet velocities of 0.4, 0.5, 0.6, 0.7, and 0.8, respectively. The η_{cell} decreases with an increased velocity of coolant as a result of decreased T_{cell}. The η_{th} is 54.84%, 54.76%, 54.66%, 54.6%, and 54.54% for the inlet velocities of 0.4, 0.5, 0.6, 0.7, and 0.8, respectively. The η_{th} decreases with an increase in coolant velocity. The η_{th} is sensitive to the temperature gain of the coolant fluid. The increase in η_{cell} with inlet velocity results in a lesser amount of heat energy available for the coolant to be carried away. Hence, the temperature gain of the coolant fluid diminishes with an increased V_{in}, leading to a marginal reduction in η_{th}.

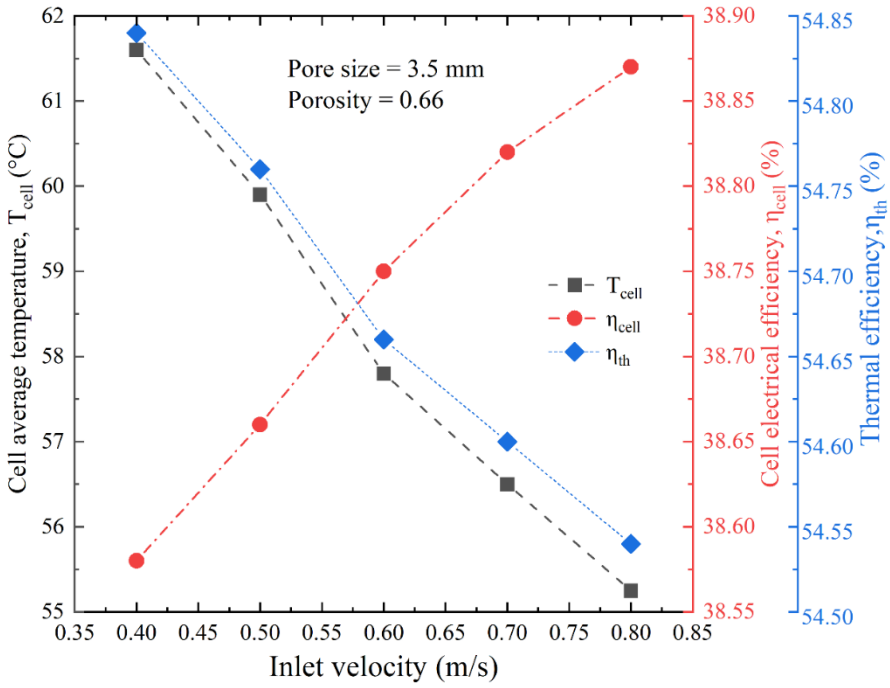


Figure 16: Variation in T_{cell}, η_{cell} and η_{th} with inlet velocity

Figure 17 shows the variation in the ΔT_{TEG} and P_{TEG} with the inlet velocity at $\phi = 0.66$ and $d_p = 3.5$ mm. The ΔT_{TEG} is 51.46 °C, 50.5 °C, 49.56 °C, 48.8 °C, and 48 °C for the inlet velocities of 0.4, 0.5, 0.6, 0.7, and 0.8, respectively. It is observed that the ΔT_{TEG} decreases with an increased V_{in}. As the V_{in} increases, the increased convective HTC at the cold junction leads to a decrease in cold junction temperature. At the same time, the higher coolant velocity also removes heat more efficiently from the adjacent heat source. This results in a reduced T_h of the TEG module. However, the reduction in hot junction temperature is higher, leading to a decreased ΔT_{TEG} with increased inlet velocity. The P_{TEG} is 5.28 W, 4.84 W, 4.51 W, 4.27 W, and 4.03 W for the inlet velocities of 0.4, 0.5, 0.6, 0.7, and 0.8, respectively. The reduced temperature gradient at higher coolant velocities contributes to the observed decline in power generation from TEG modules. The η_{TEG} also decreases from 1.44% to 1.21% for an increase in velocity from 0.4 m/s to 0.8 m/s, respectively.

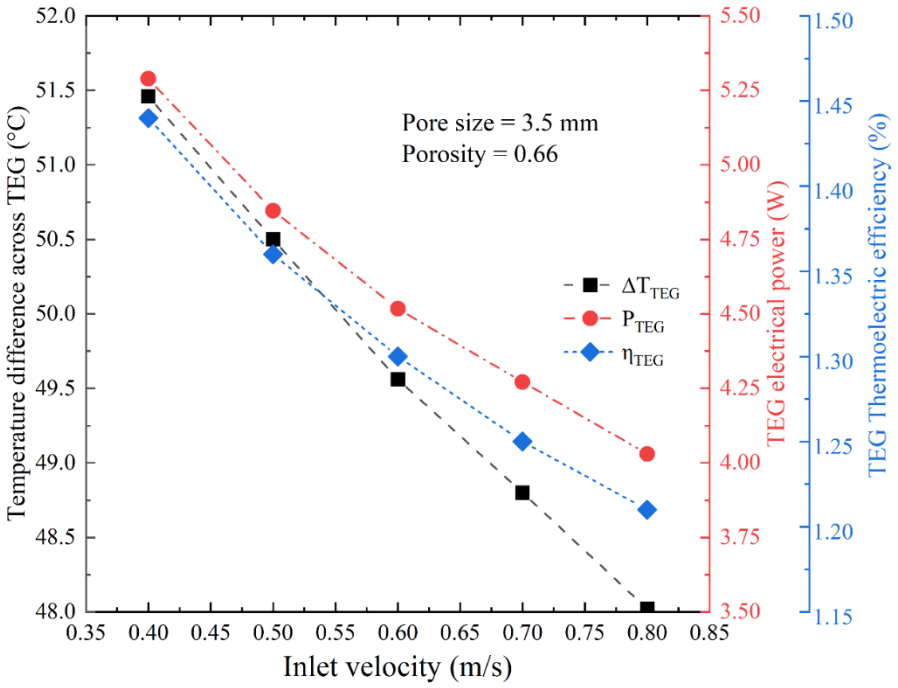


Figure 17: Variation in ΔT_{TEG}, P_{TEG}, and η_{TEG} with inlet velocity

Figure 18 shows the variation in ζ_{el}, ζ_{th}, and ζ_o with the inlet velocity at $\phi = 0.66$, and $d_p = 3.5$ mm. The ζ_{el} is 37.62%, 37.08%, 36.44%, 35.65%, and 34.31% for the inlet velocities of 0.4, 0.5, 0.6, 0.7, and 0.8, respectively. The ζ_{el} decreases with an increase in coolant inlet velocity. The P_{el} increases with an increased inlet velocity. However, the benefits are offset by increased pumping power losses and a drop in P_{TEG}, leading to an unfavourable trade-off. The ζ_{th} is 15.14%, 15.1%, 15.05%, 15.01%, and 14.98% for the inlet velocities of 0.4, 0.5, 0.6, 0.7, and 0.8, respectively. The ζ_{th} is marginally affected by the inlet velocity of the coolant fluid. A comparison of Figures 16 and 14 suggests that out of 54.84% of the thermal power, only 15.14% can be converted into useful work. This disparity arises because the recovered thermal energy is available at relatively low temperatures, which limits its potential to perform useful work. The ζ_o is found to decrease progressively with increasing coolant inlet velocity, with values of 52.76%, 52.18%, 51.49%, 50.66%, and 49.29% corresponding to inlet velocities of 0.4, 0.5, 0.6, 0.7, and 0.8 m/s, respectively. This declining trend indicates that while beneficial for heat removal, higher coolant velocities result in a net reduction in the system's ability to convert available energy into useful work. Therefore, from an exergy optimization perspective,

lower coolant velocities are preferable for the thermal management of the HCPV-T system studied. However, as shown in Figure 15, the T_{max} exceeds the safe operational limit of 110 °C at V_{in} = 0.4 m/s. This implies that the lowest velocity, though optimal in terms of exergy, fails to maintain the thermal safety of the system. Hence, the optimal inlet velocity must balance both thermal regulation and exergy efficiency and lie between 0.4 m/s and 0.5 m/s at ϕ = 0.66, and d_p = 3.5 mm.

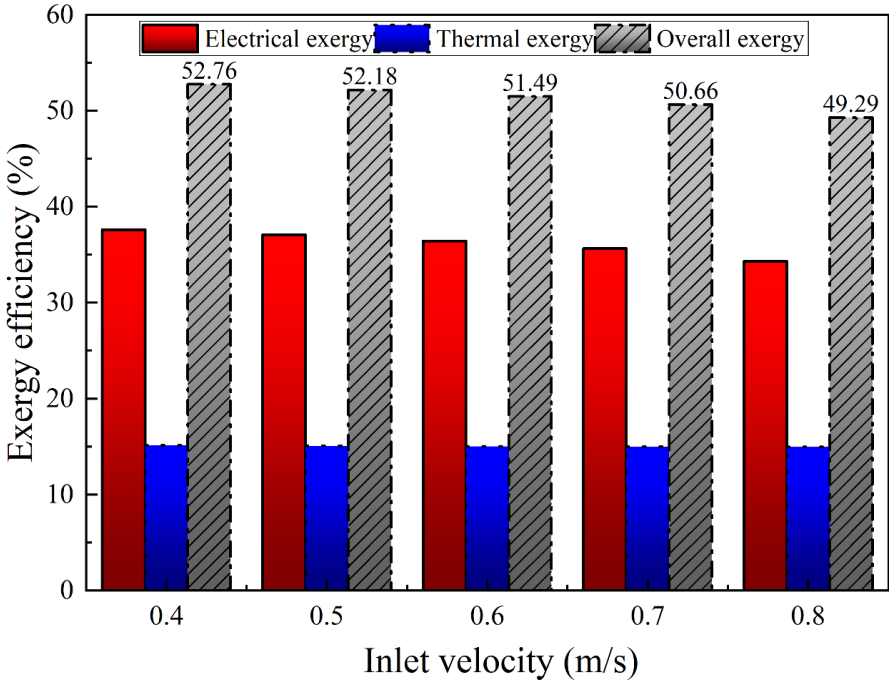


Figure 18: Variation in ζ_{el}, ζ_{th}, and ζ_o with inlet velocity

5. Conclusions

The performance of a highly concentrated photovoltaic-thermal (HCPV-T) system integrated with an aluminium porous heat sink, a thermoelectric generator (TEG) module, and a spectral splitter is evaluated in the current study. The thermoelectric module enhances the overall exergy efficiency by converting the excess waste heat into useful electrical energy output. The influence of key parameters, such as porosity of the heat sink, pore size, and coolant inlet velocity, on the performance characteristics of both the Thermoelectric module and the HCPV-T system is investigated. The proposed hybrid cooling approach can maintain the cell

temperature under a critical threshold of 110 °C under high concentration. In particular, porosities in the range of 0.75-0.8 achieve a favourable balance between thermal regulation and pumping power, while porosities above 0.8 cause excessive cell temperature and thermal stresses, making them unsuitable for thermal regulation in such systems. A minimum coolant inlet velocity of 0.5 m/s is recommended to ensure safe operating temperatures, though very high inlet velocities reduce the overall exergy efficiency due to increased hydraulic losses. Pore size had a minor influence on the cell temperature and electrical efficiency; however, the pressure drop increases sharply at smaller pore sizes. The thermal stress variation suggests that the thermal stress maximizes at the TEG locations, while it is lowest at the centre and corners of the cell. The maximum thermal stress exceeds the yield limit of the PV cell for the porosities of 0.85 and 0.9. The failure index of the porous structure is also reported in the current study, suggesting that the structure is mechanically safe for all the input parameters. Hence, in designing the cooling strategies of such systems, one should (1) select moderate porosities (~0.75-0.8), (2) maintain coolant velocities above 0.5 m/s but avoid excessive flow rates, and (3) limit operating conditions to keep stress levels below the material limits. These will ensure efficient thermal management, reliable electrical performance, and mechanical safety. The insights of this study provide a foundational basis for the design and optimization of the HCPV-T systems. Future work will focus on experimental validation of the integrated system, benchmarking against alternative cooling strategies, and a multi-parameter optimization to further establish the feasibility and competitiveness of the proposed approach.

Data Availability

The data that support the findings of this study are available from the corresponding author upon reasonable request.

Acknowledgements

We would like to express our appreciation to the Department of Science and Technology (DST), India, for their visionary support through grant number TAR/2020/000358, which played a crucial role in the successful completion of this research. We thank the TIH-DST funding (RD/0125-TIHIR18-005) for supporting these research activities. We also gratefully acknowledge the European Union's Horizon 2020 Research and Innovation Programme for its valuable support via the Marie Skłodowska-Curie Individual Fellowship (grant agreement no. 101028904-NANOSPLIT-H2020-MSCA-IF-2020), which provided essential resources and fostered scientific growth. Additionally, we sincerely thank the Horizon Europe program for its generous assistance under Grant Agreement ID: 101152661, as part of the HORIZON-TMA-MSCA-PF-EF European Fellowships. This esteemed funding was instrumental in advancing our research and exploring new frontiers. The collective support from these respected organizations has been fundamental to the success of this work, and we remain deeply thankful.

References:

[1] Gupta A, Chougule SS, Saha SK. Cooling of highly concentrated photovoltaic cells with confined jet impingement by introducing channel configurations. Renew Energy 2024;237:121600. https://doi.org/10.1016/j.renene.2024.121600.

[2] Nishioka K, Takamoto T, Agui T, Kaneiwa M, Uraoka Y, Fuyuki T. Annual output estimation of concentrator photovoltaic systems using high-efficiency InGaP/InGaAs/Ge triple-junction solar cells based on experimental solar cell's characteristics and field-test meteorological data. Sol Energy Mater Sol Cells 2006;90:57–67. https://doi.org/10.1016/j.solmat.2005.01.011.

[3] Fallah Kohan HR, Lotfipour F, Eslami M. Numerical simulation of a photovoltaic thermoelectric hybrid power generation system. Sol Energy 2018;174:537–48.

https://doi.org/10.1016/j.solener.2018.09.046.

[4] Gupta A, Chougule SS, Saha SK. Thermal Management Of Highly Concentrated Photovoltaic-Thermal System Using Confined Jet Impingement And Thermoelectric Generator 2024:1–8. https://doi.org/https://doi.org/10.11159/icaera24.135.

[5] Chougule SS, Sahu SK. Performance of carbon nanotubes-water nanofluid charged wickless heat pipe flat plate solar collectors having different filling ratio. J Sol Energy Eng Trans ASME 2015;137:1–4. https://doi.org/10.1115/1.4028701.

[6] Barewar SD, Chougule SS, Jadhav J, Biswas S. Synthesis and thermo-physical properties of water-based novel Ag/ZnO hybrid nanofluids. J Therm Anal Calorim 2018;134:1493–504. https://doi.org/10.1007/s10973-018-7883-6.

[7] Gupta A, Chougule SS, Saha SK. Numerical simulation on thermal management of concentrating photovoltaic-thermal module with confined jet impingement with Ag-ZnO hybrid nanofluids 2023:547–55.

[8] Dwivedi P, Sudhakar K, Soni A, Solomin E, Kirpichnikova I. Advanced cooling techniques of P.V. modules: A state of art. Case Stud Therm Eng 2020;21:100674. https://doi.org/10.1016/j.csite.2020.100674.

[9] Moiz M, Vadlamudi SRG, Srivastava A. Comprehensive experimental thermal analysis of single bubble nucleation in vertical flow boiling: Whole field temperature and microlayer dynamics. Int J Heat Mass Transf 2024;233:126006. https://doi.org/10.1016/j.ijheatmasstransfer.2024.126006.

[10] Barewar SD, Joshi M, Sharma PO, Kalos PS, Bakthavatchalam B, Chougule SS, et al. Optimization of jet impingement heat transfer: A review on advanced techniques and parameters. Therm Sci Eng Prog 2023;39:101697. https://doi.org/10.1016/j.tsep.2023.101697.

[11] Kiwan SM, Khlefat AM. Thermal cooling of photovoltaic panels using porous material.

Case Stud Therm Eng 2021;24:100837. https://doi.org/10.1016/j.csite.2020.100837.

[12] Chen WH, Wang CC, Hung CI, Yang CC, Juang RC. Modeling and simulation for the design of thermal-concentrated solar thermoelectric generator. Energy 2014;64:287–97. https://doi.org/10.1016/j.energy.2013.10.073.

[13] Sabry M, Lashin A, Al Turkestani M. Experimental and simulation investigations of CPV/TEG hybrid system. J King Saud Univ - Sci 2021;33:101321. https://doi.org/10.1016/j.jksus.2020.101321.

[14] Li W, Shi Y, Chen K, Zhu L, Fan S. A Comprehensive Photonic Approach for Solar Cell Cooling. ACS Photonics 2017;4:774–82. https://doi.org/10.1021/acsphotonics.7b00089.

[15] Zhu L, Raman A, Wang KX, Anoma MA, Fan S. Radiative cooling of solar cells. Optica 2014;1:32. https://doi.org/10.1364/optica.1.000032.

[16] Theristis M, O'Donovan TS. Electrical-thermal analysis of III-V triple-junction solar cells under variable spectra and ambient temperatures. Sol Energy 2015;118:533–46. https://doi.org/10.1016/j.solener.2015.06.003.

[17] Barewar SD, Tawri S, Chougule SS. Heat transfer characteristics of free nanofluid impinging jet on flat surface with different jet to plate distance: An experimental investigation. Chem Eng Process - Process Intensif 2019;136:1–10. https://doi.org/10.1016/j.cep.2018.12.001.

[18] Royne A, Dey CJ. Design of a jet impingement cooling device for densely packed PV cells under high concentration. Sol Energy 2007;81:1014–24. https://doi.org/10.1016/j.solener.2006.11.015.

[19] Masalha I, Masuri SU, Badran O, Alahmer A. A multi-method approach to investigating porous media cooling for enhanced thermal performance of photovoltaic panels: Exploring the effects of porosity, flow rates, channel design, and coolant types. Int J

Thermofluids 2025;27:101165. https://doi.org/10.1016/j.ijft.2025.101165.

[20] Salman AHA, Hilal KH, Ghadhban SA. Enhancing performance of PV module using water flow through porous media. Case Stud Therm Eng 2022;34. https://doi.org/10.1016/j.csite.2022.102000.

[21] Poudel S, Zou A, Maroo SC. Thermal Management of Photovoltaics Using Porous Nanochannels. Energy and Fuels 2022;36:4549–56. https://doi.org/10.1021/acs.energyfuels.2c00305.

[22] Zhao B, Hu M, Ao X, Xuan Q, Pei G. Spectrally selective approaches for passive cooling of solar cells: A review. Appl Energy 2020;262:114548. https://doi.org/10.1016/j.apenergy.2020.114548.

[23] Yusuf A, Ballikaya S. Performance analysis of concentrated photovoltaic systems using thermoelectric module with phase change material. J Energy Storage 2023;59. https://doi.org/10.1016/j.est.2022.106544.

[24] Chougule SS, Sahu SK. Thermal performance of nanofluid charged heat pipe with phase change material for electronics cooling. J Electron Packag 2015;137:1–7. https://doi.org/10.1115/1.4028994.

[25] Gupta A, Chougule SS, Saha SK. Advanced cooling strategies for highly concentrated PV-T systems : Confined jet impingement , thermoelectric generator integration with channel configurations. Renew Energy 2025;254:123664. https://doi.org/10.1016/j.renene.2025.123664.

[26] Barrau J, Rosell J, Chemisana D, Tadrist L, Ibañez M. Effect of a hybrid jet impingement/micro-channel cooling device on the performance of densely packed PV cells under high concentration. Sol Energy 2011;85:2655–65. https://doi.org/10.1016/j.solener.2011.08.004.

[27] Shaeli MN, Jalil JM, Baccar M. Improving the performance of solar photovoltaic

thermal cells using jet impingement and phase change materials cooling technology. Renew Energy 2024;227:120536. https://doi.org/10.1016/j.renene.2024.120536.

[28] Khalili Z, Sheikholeslami M. Analyzing the effect of confined jet impingement on efficiency of photovoltaic thermal solar unit equipped with thermoelectric generator in existence of hybrid nanofluid. J Clean Prod 2023;406:137063. https://doi.org/10.1016/j.jclepro.2023.137063.

[29] Huaxu L, Fuqiang W, Dong Z, Ziming C, Chuanxin Z, Bo L, et al. Experimental investigation of cost-effective ZnO nanofluid based spectral splitting CPV/T system. Energy 2020;194:116913. https://doi.org/10.1016/j.energy.2020.116913.

[30] Aldossary A, Mahmoud S, Al-Dadah R. Technical feasibility study of passive and active cooling for concentrator PV in harsh environment. Appl Therm Eng 2016;100:490–500. https://doi.org/10.1016/j.applthermaleng.2016.02.023.

[31] Https://customthermoelectric.com/1261g-7l31-04cqthermoelectric-, Generator-40-x-40mm.html. Commercial TEG 1261G-7L31-04CQ data sheet, manufactured by Custom Thermoelectric

[32] Abo-Zahhad EM, Ookawara S, Radwan A, El-Shazly AH, ElKady MF. Thermal and structure analyses of high concentrator solar cell under confined jet impingement cooling. Energy Convers Manag 2018;176:39–54. https://doi.org/10.1016/j.enconman.2018.09.005.

[33] Javidan M, Moghadam AJ. Experimental investigation on thermal management of a photovoltaic module using water-jet impingement cooling. Energy Convers Manag 2021;228. https://doi.org/10.1016/j.enconman.2020.113686.

[34] Hasan O, Arif AFM, Siddiqui MU. Finite element modeling, analysis, and life prediction of photovoltaic modules. J Sol Energy Eng Trans ASME 2014;136. https://doi.org/10.1115/1.4026037.

[35] ASTM G173-03(2012), Standard Tables for Reference Solar Spectral Irradiances: Direct Normal and Hemispherical on 37° Tilted Surface, ASTM International, West Conshohocken, PA, 2012. [Available online: https://www.nrel.gov/grid/solar-resource/spectra-am1.5

[36] 3C44A – with 10×10 mm2Concentrator Triple Junction Solar cell. http://www.azurspace.com 2016:1–6.

[37] Sharma S, Talukdar P. Thermo-mechanical analysis of a porous volumetric solar receiver subjected to concentrated solar radiation. Sol Energy 2022;247:41–54. https://doi.org/10.1016/j.solener.2022.10.014.

[38] Mahmoudi Y. Effect of thermal radiation on temperature differential in a porous medium under local thermal non-equilibrium condition. Int J Heat Mass Transf 2014;76:105–21. https://doi.org/10.1016/j.ijheatmasstransfer.2014.04.024.

[39] Lu W, Zhao CY, Tassou SA. Thermal analysis on metal-foam filled heat exchangers. Part I: Metal-foam filled pipes. Int J Heat Mass Transf 2006;49:2751–61. https://doi.org/10.1016/j.ijheatmasstransfer.2005.12.012.

[40] Ahmed M, Radwan A. Performance evaluation of new modified low-concentrator polycrystalline silicon photovoltaic/thermal systems. Energy Convers Manag 2017;149:593–607. https://doi.org/10.1016/j.enconman.2017.07.057.

[41] Zimmermann S, Helmers H, Tiwari MK, Paredes S, Michel B, Wiesenfarth M, et al. A high-efficiency hybrid high-concentration photovoltaic system. Int J Heat Mass Transf 2015;89:514–21. https://doi.org/10.1016/j.ijheatmasstransfer.2015.04.068.

[42] Evans AG, Hutchinson JW. The thermomechanical integrity of thin films and multilayers. Acta Metall Mater 1995;43:2507–30. https://doi.org/10.1016/0956-7151(94)00444-M.

[43] Souare PM, Sylvestre J. Thermal and mechanical analysis of a concentrated photovoltaic

module with integrated secondary optics. AIP Conf Proc 2016;1766. https://doi.org/10.1063/1.4962114.

[44] Aichmayer L, Spelling J, Laumert B. Preliminary design and analysis of a novel solar receiver for a micro gas-turbine based solar dish system. Sol Energy 2015;114:378–96. https://doi.org/10.1016/j.solener.2015.01.013.

[45] Lin J, Liao T, Lin B. Performance analysis and load matching of a photovoltaic-thermoelectric hybrid system. Energy Convers Manag 2015;105:891–9. https://doi.org/10.1016/j.enconman.2015.08.054.

[46] Zhang Z, Li W, Kan J. Behavior of a thermoelectric power generation device based on solar irradiation and the earth's surface-air temperature difference. Energy Convers Manag 2015;97:178–87. https://doi.org/10.1016/j.enconman.2015.03.060.

[47] Bitschi A. Modelling of thermoelectric devices for electric power generation 2009:144.

[48] Evola G, Marletta L. Exergy and thermoeconomic optimization of a water-cooled glazed hybrid photovoltaic/thermal (PVT) collector. Sol Energy 2014;107:12–25. https://doi.org/10.1016/j.solener.2014.05.041.

Appendix A. Effect of spectral splitter configuration on cell temperature

A1. Cell temperature without the spectral splitter

Figure A1 illustrates the temperature distribution on the top surface of the PV cell in the absence of the spectral splitter, under conditions of ϕ = 0.66, d_p = 3.5 mm, and an inlet velocity of 0.8 m/s. Without the spectral splitter, the T_{max} rises to 139.5 °C. This increase is attributed to the full solar spectrum directly incident on the PV cell, including longer wavelengths that contribute significantly to thermal loading. As a result, the T_{max} exceeds the operational limit of 110 °C, highlighting the critical role of the spectral splitter. This elevated temperature compromises the electrical efficiency of the PV cell and raises concerns regarding material reliability and long-term stability. The comparison emphasizes the necessity of spectral splitting to filter out excess thermal radiation and maintain the PV cell within safe operating limits.

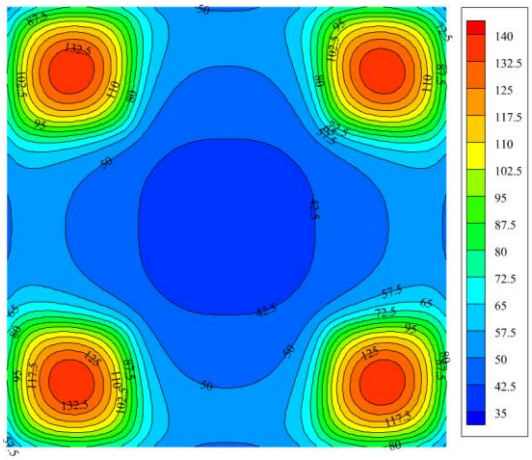


Figure A1. Temperature distribution over the PV cell top surface without a spectral splitter

A2. Cell temperature when the splitter is in direct thermal contact with the PV cell

Figure A2 illustrates the temperature distribution on the top surface of the PV cell, when the splitter is placed in direct thermal contact with the PV cell surface under conditions of ϕ = 0.66, d_p = 3.5 mm, and an inlet velocity of 0.8 m/s. This temperature distribution is shown to compare

two cases: case 1, when a gap is maintained between the spectral splitter and PV cell, and case 2, when the spectral splitter is in direct thermal contact with the PV cell. A comparison of Figures 5(f) and A2 reveals that the temperature distribution is nearly identical for both cases. However, the T_{max} is observed to be 103.7 °C in case 2, which is marginally higher, i.e. 0.2 °C, than in case 1. This slight increase is attributed to the low thermal conductivity of the spectral splitter. As the gap between the splitter and the PV cell increases, the thermal influence of the splitter on system performance becomes even less significant. Therefore, the assumption of neglecting the thermal interaction between the splitter and PV cell is considered valid for the present study.

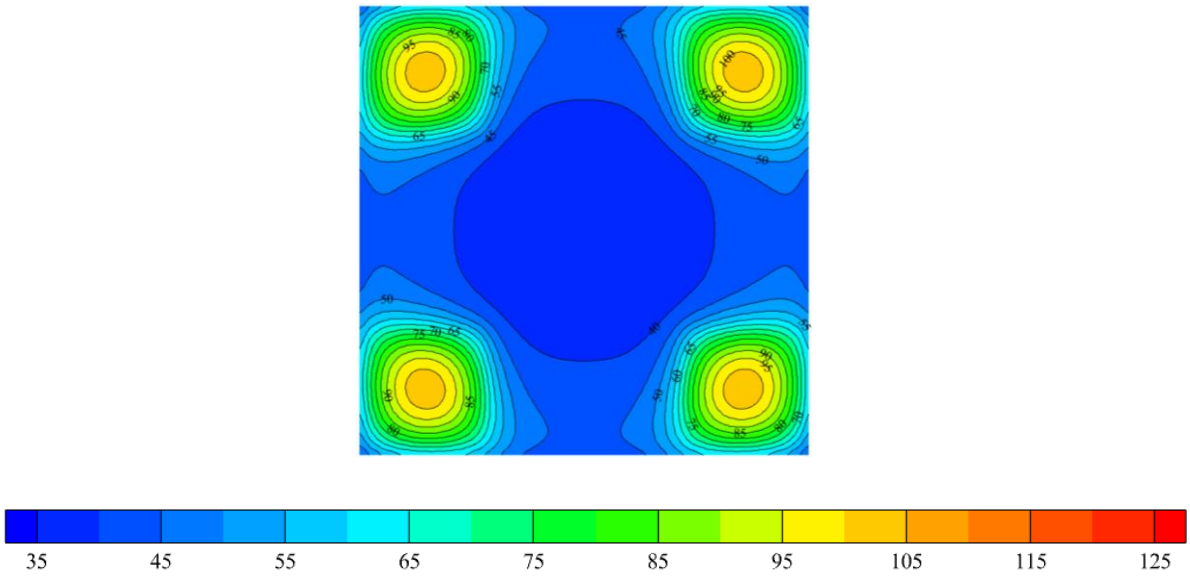


Figure A2. Temperature distribution over the PV cell top surface, when the splitter is attached to the PV cell top surface